Noble gas and nitrogen investigation of the unique andesitic achondrite Erg Chech 002: Degassing, cosmic ray exposure and radiogenic ingrowth histories

D. J. Byrne[1*], M. W. Broadley[2], E. Füri[3], L. Tissandier[3], L. Zimmermann[3], M. G. Almayrac[2], D. V. Bekaert[3], J. A. Barrat[4] and B. Marty[3]

[1]Wairakei Research Centre, GNS Science, Taupō 3384, New Zealand

* Corresponding author email: d.byrne@gns.cri.nz

[2] Department of Earth and Environmental Science, University of Manchester, UK

[3] Université de Lorraine, CNRS, CRPG, Nancy, France

[4] Univ Brest, CNRS, IRD, Ifremer, LEMAR, F-29280 Plouzané, France

For submission to GCA

Number of Words = 7,122

Number of Figures = 9

Number of Tables = 5

14th of October, 2024

Abstract = 494 words

Erg Chech 002 (EC 002) is a unique achondrite that represents a fragment of the igneous crust of an extinct protoplanet that accreted within the first million years of solar system evolution (Barrat et al., 2021). Assessing the extent of volatile depletion in EC 002 has the potential to provide information regarding volatile loss processes during formation of the earliest differentiated planetary bodies in the solar system. In order to determine the amounts of trapped "planetary" noble gas components that have been preserved in EC 002 during formation of its parent body and evaluate the extent of degassing of the EC 002 parent body, we present a comprehensive noble gas and nitrogen isotope analysis of EC 002 using several different extraction techniques. Bulk noble gas composition, determined through step heating, reveals strongly cosmogenic He and Ne isotopes ($^{3}He/^{4}He$ = 0.00731 ± 0.00007; $^{20}Ne/^{22}Ne$ = 0.768 ± 0.002; $^{21}Ne/^{22}Ne$ = 0.846 ± 0.015), cosmogenic enrichments in $^{38}Ar/^{36}Ar$, and Kr and Xe isotopic spectra, as well as a strong enrichment in radiogenic ^{40}Ar ($^{40}Ar/^{36}Ar$ = 5523 ± 42). Individual temperature step extractions show preferential release of radiogenic ^{40}Ar and cosmogenic ^{21}Ne at lower temperature steps, both indicative of selective release from the K, Na-rich plagioclase phases. Laser ablation analyses of individual grains confirm this heterogeneous noble gas distribution, and show that the vast

majority of He and Ne is hosted in the pyroxene grains. Substantial loss of cosmogenic He and Ne from the plagioclase phases via diffusion, even at low temperatures, is required to explain this observation. Conversely, radiogenic ^{40}Ar is strongly concentrated in the plagioclase phases, corroborating step-heating observations. Further evidence of He loss is demonstrated by the discordant (U-Th)/He age of 2700 Myr, yet the K-Ar age of 4530^{+12}_{-13} Myr is in agreement with the reported ^{26}Al-^{26}Mg formation age, precluding significant thermal events occurring long after the formation of EC 002. Cosmogenic ^{38}Ar and ^{21}Ne abundances in individual pyroxene grains yield a cosmic ray exposure age range of 27 - 41 Myr, with a preferred age of 35 Myr. Step-crushing data show excesses in fissiogenic heavy Xe isotopes, with a fissiogenic spectrum most compatible with U fission as opposed to Pu. Trapped "primordial" noble gas abundances are difficult to distinguish from the high cosmogenic and radiogenic contributions, but are at least an order of magnitude lower than typical non-carbonaceous chondrites that EC 002 is thought to be derived from, suggesting relatively extensive degassing. Bulk nitrogen isotope ratio (δ^{15}N = +15.0 ± 0.5 ‰) is within the range expected for ordinary chondrites (OC) and distinct from the other possible non-carbonaceous chondrite class, the enstatite chondrites. The bulk ^{36}Ar/N ratio is lower than typical OC values, although it is consistent with fractionation during degassing of a parent body with an initially OC-like composition. Overall this constrains the origin of the volatile inventory of the EC 002 parent body, and provides evidence for degassing processes occurring on planetary bodies at the earliest stages of solar system history.

1. Introduction

Discovered in Algeria in the spring of 2020, Erg Chech 002 (EC 002) is a unique meteorite that represents part of the primordial igneous crust of an extinct protoplanet (Barrat et al., 2021). It is a remnant of a differentiated planetary body from the early solar system, which were likely important building blocks for the terrestrial planets. EC 002 consists primarily of ~mm size pyroxene grains (38 modal %) enclosed by a groundmass of plagioclase feldspar (45 modal %) and interstitial silica minerals (5 modal %), with minor contributions from accessory minerals including chromite, ilmenite, sulfide and iron metal (Barrat et al., 2021). It also displays sporadic pyroxene megacrysts up to several cm in size, and its texture suggests crystallisation within a thick flow or in a shallow intrusion, with a relatively short cooling history (Barrat et al., 2021). Whilst EC 002 does share some compositional similarities with other high-Si achondrites such as GRA 06128/9 and NWA 11119 (Day et al., 2009; Srinivasan et al., 2018), it differs in its low and highly fractionated siderophile element abundances, clearly demonstrating that unlike these previously studied andesitic achondrites, it derives from a differentiated parent body. Incompatible trace element abundances indicate that this lava derives from the partial melting of a non-carbonaceous chondritic reservoir, at a high degree of melting of around 25% (Chaussidon et al., 2021).

With a ^{26}Al-^{26}Mg crystallization age of 4565 Myr (i.e. 1.80 ± 0.01 Myr after the formation of CAI's, the oldest known solar system materials), EC 002 represents the oldest felsic magmatic rock identified to date (Fang et al., 2022). Several other radioisotope dating techniques have since produced consistent results, including ^{53}Mn-^{53}Cr (Anand et al., 2022), ^{40}K-^{40}Ca (Dai et al., 2023), and Ar-Ar (Takenouchi et al., 2021). Differentiation of

the EC 002 parent body might have taken place significantly before, possibly during the first Myr after start of solar system formation. Protoplanets covered by andesitic crusts were probably frequent, but no asteroid shares the spectral features of EC 002 (Barrat et al., 2021), suggesting that almost all of these bodies have disappeared, either because they went on to form the building blocks of larger bodies or planets or were simply destroyed.

EC 002 offers a rare window into understanding early planetary formation processes, contemporaneous with the formation of the cores of the parent bodies of iron meteorites (Kruijer et al., 2014; Spitzer et al., 2021). In particular, it may provide an opportunity to investigate the behavior of highly volatile elements such as noble gases during differentiation of a primitive body. Noble gas isotopes are a powerful tool for investigating a number of cosmochemical processes, including volatile provenance (Bekaert et al., 2019), planetary degassing, volatile radiogenic isotope retention, and cosmic ray exposure (Leya et al., 2013; Broadley et al., 2020a).

One of the key uses of noble gas isotope analyses in meteorites is to investigate the cosmic ray exposure (CRE) age as recorded by the accumulation of cosmogenic isotopes produced by spallation reactions from cosmic rays of either galactic (GCR) or solar (SCR) origin. These ages are typically considered to represent the duration between breakup of a larger parent body and the transit of the meteorite to Earth (Scherer and Schultz, 2000; Meier et al., 2018; Bekaert et al., 2022). In samples from the early solar system they can also be used to infer potential differences in the irradiation conditions of the protosolar nebula (Riebe et al., 2017). The application of cosmogenic noble gas isotope techniques to igneous rocks such as EC 002 however may be complicated due to incomplete retention of light noble gases particularly in silica-rich phases, as well as the potential concentration of non-radiogenic noble gases in vesicles or along grain boundaries. These issues may not be apparent when using conventional bulk sample analysis such as step-heating.

Light noble gas isotope data (He, Ne and Ar) obtained using step-heating extraction for EC 002 was previously reported in Barrat et al. (2021) and used to determine cosmogenic exposure age and for radiogenic Ar analysis. In this manuscript we present a comprehensive noble gas and nitrogen isotope analysis of EC 002 (He, Ne, Ar, Kr, Xe), using three separate extraction techniques for noble gas analysis: step heating, crushing, and laser ablation, with nitrogen analysis extraction by laser heating. The results of these analyses reveal some intricacies in the cosmogenic noble gas isotope composition of EC 002 that was not apparent in the step-heating data reported by Barrat et al. (2021) and prompts a re-evaluation of the cosmic ray exposure history of the sample. We also investigate the radiogenic isotope composition of the different mineral phases present within EC 002, and discuss the primordial volatile signature and degassing history.

2. Methodology

2.1 Extraction

Three extraction techniques were used for noble gas analysis. These provide complementary information regarding the distribution of noble gases within EC 002, as well as the production and retention/loss of radiogenic and cosmogenic isotopes from different mineral phases. Step heating extractions provide a precise

determination of bulk noble gas composition, and individual heating steps can be associated with different mineral phases, due to their differing thermal sensitivity to diffusive loss (Futagami et al., 1993). Crushing analyses are used to identify the composition of noble gases situated within inclusions and along grain boundaries. In-situ laser ablation analyses can be used to target individual mineral grains within the sample, and can be combined with SEM analysis regarding the target material's chemical composition.

2.1.1 Step-heating

Step heating analysis was performed using a filament furnace, with samples heated directly in alumina-coated tungsten evaporation baskets (Ted Pella Inc.). All baskets were degassed under vacuum at 1600°C for 10 minutes prior to use. A sample fragment of mass 8.3 mg was loaded into one basket, with an additional empty basket used to determine blanks at each temperature step. Prior to analysis the entire furnace including samples and blanks was baked under vacuum at 150°C for 24 hours to remove atmospheric contributions. Sample gas was released by passing a current through the basket, following a previously determined temperature calibration (Bekaert et al., 2018; Broadley et al., 2020b). Extractions were performed at temperature intervals of 200°C between 600°C and 1400°C, at which point the sample was observed to have melted. An additional re-extraction at 1600°C was undertaken to confirm that all gas had been released.

2.1.2 Crushing

Crushing analysis was performed using a custom-built stainless steel piston crusher, with pressure applied using a hydraulic ram. A sample mass of 185.2 mg was loaded into the crusher. Prior to analysis the crushing apparatus including sample was baked under vacuum at 150°C for 24 hours and subsequently pumped for a further 48 hours until blanks were low and reproducible. Gas was then released from the sample during crushing step 1 by applying pressure until audible cracking was heard. Subsequent crushing steps were performed by sequentially increasing the pressure for a total of 4 step crushes.

2.1.3 Laser Ablation

Laser ablation analysis was performed using a Nd:YAG 213 nm laser (Elemental Scientific NWR213). A polished thick section of sample was loaded into a windowed ultra-high vacuum chamber and baked at 150°C for 24 hours. The sample chamber was then pumped for a further 48 hours until blanks were low and reproducible. Ablations were performed using a laser fluence of 12 Jcm^{-2} and spot diameter of 110 µm. Each ablation consisted of 200 pulses at a repetition rate of 10 Hz. For each analysis an array of between 8 to 20 spots were ablated in order to provide sufficient gas for measurement. Five analyses were targeted within individual pyroxene grains (labelled Px1-5), whilst a single additional analysis was targeted within the plagioclase-dominated groundmass (Plag1). After the analyses were completed, the sample was removed from the chamber and the ablation volumes were calculated using an optical interferometer (Zygo ZeGage ProHR). Average ablation depth was ~20 µm, resulting in a typical ablated mass of ~1µg per spot. Bulk chemical compositions of the individual minerals analysed were also determined after noble gas analysis, using the Jeol-JSM 6510 scanning electron microscope (SEM) coupled with an energy dispersive X-ray spectroscopy (EDS) system, located at CRPG.

The EDS XFlash 5030 detector from Bruker is running with the Esprit 2.2 software. The spectra were acquired with a 15kV acceleration voltage and virtual controls were used for the element quantifications.

2.2 Purification

Sample gas extracted using step heating and laser ablation techniques was passed through a preliminary purification stage using an inline Ti-sponge getter operated at 650°C for 10 minutes. This step was bypassed for the crushing analyses in order to exclude the higher blanks associated with this hot getter. The subsequent analytical procedure is the same for each extraction technique. Firstly the sample gas was exposed to dual Ti-Sponge getters held at 550°C for 10 minutes. An activated carbon cold finger cooled using liquid nitrogen was then used to trap Ar, Kr and Xe, before the remaining He and Ne were trapped onto a activated charcoal cryogenic trap held at ~10 K.

The noble gases were then sequentially released before being inlet into the mass spectrometer for analysis. A final purification stage consisting of dual Ti-sponge getters at room temperature was also applied here to remove any remaining reactive gases. Helium was released from the cryogenic trap at 34K, and neon was subsequently released at 90K. For step heating and crushing analyses, Ar, Kr and Xe were released simultaneously from the activated carbon cold finger before Kr and Xe were immediately retrapped using a quartz cold finger cooled with liquid nitrogen. For laser ablation analyses insignificant quantities of the heavy noble gases were present and so this step was omitted and Ar simply inlet directly into the mass spec. Finally, Kr and Xe were released from the quartz cold finger at room temperature and inlet for simultaneous measurement.

2.3 Noble gas analysis

All analysis was performed using a Helix MC Plus mass spectrometer (Thermo Fisher Scientific). Helium analysis was performed using peak jumping, with ^{4}He measured on a Faraday cup and ^{3}He on a compact discrete dynode (CDD) electron multiplier in pulse counting mode. Neon analysis was performed using multicollection for simultaneous measurement of all 3 isotopes using CDD detectors. An activated carbon cold finger at liquid nitrogen temperature was left open to the spectrometer during Ne measurements in order to minimise interference from $^{12}C^{16}O_2^{++}$ on $^{22}Ne^{+}$ peaks. CO_2^{+} levels were monitored during analysis and ^{22}Ne signals were subsequently corrected using a calibrated CO_2^{++}/CO_2^{+} ratio. $^{40}Ar^{++}$ was fully resolved from $^{20}Ne^{+}$, and so no correction was required. Ar was measured using a peak jumping procedure with ^{40}Ar measured using a Faraday cup and ^{36}Ar, ^{38}Ar on CDD detectors. Xe and Kr were inlet together and Kr was analysed directly after the Xe measurement was completed. Both Xe and Kr were analysed using a peak jumping procedure with all isotopes measured on CDD detectors (Bekaert et al. 2018; Broadley et al. 2020b).

Standards were run daily following the same separation procedure as sample analyses. For this purpose, a high $^{3}He/^{4}He$ HESJ standard was used (Matsuda et al., 2002), as well as internally calibrated atmospheric combined Ne-Ar and Kr-Xe standards. All uncertainties are 1 sigma. Typical standard reproducibility was 0.36% for $^{3}He/^{4}He$, 0.58% for $^{20}Ne/^{22}Ne$, 0.41% for $^{21}Ne/^{22}Ne$, 0.31% for $^{40}Ar/^{36}Ar$, and 0.22% for $^{38}Ar/^{36}Ar$.

Blank contributions were routinely subtracted from all analyses. For laser ablation measurements, blank contributions for ^{3}He, ^{21}Ne and ^{40}Ar were 6.6 x10^{-18}, 2.8 x10^{-19} and 2.1 x10^{-15} mols respectively. For the five pyroxene analyses this represents a <6% contribution for ^{3}He and a <2% contribution for ^{21}Ne. Due to the low abundance and high variability of Ar analyses, it represents a range from 5-70% contribution for ^{40}Ar. Conversely, the plagioclase analysis has low contributions for ^{40}Ar (<1%) and ^{21}Ne (<7%), but relatively high blank contribution for ^{3}He (72%). For the step heating measurements, blanks for each isotope at each temperature step were determined by heating the blank basket to the same temperature steps as the sample. Blank contributions for ^{3}He and ^{21}Ne were <1%. For ^{40}Ar, blank contributions were higher for the 600°C and 1400°C release steps, due to the relatively low amounts of gas released, giving blank contributions of 27% and 31% respectively. For all other temperature steps the blank contribution to ^{40}Ar was <2%. Blank contributions for step heating analysis of Kr and Xe were significant for the three heating steps at which resolvable signals were obtained, with ^{84}Kr blanks ranging from 1.7 x10^{-17} mol to 3.4 x10^{-17} mol, and ^{130}Xe ranging from 2.7 x10^{-19} mol to 3.9 x10^{-19} mol. This represents <40% of the sample signal in all cases however. For crushing analyses, blank levels for ^{4}He, ^{20}Ne, ^{40}Ar, ^{84}Kr and ^{130}Xe were 2.9 x10^{-15} mol, 4.7 x10^{-17} mol, 1.8 x10^{-15} mol, 2.0 x10^{-18} mol and 4.0 x10^{-20} mol respectively. Respectively this resulted in a maximum blank contribution of 3%, 28%, 0.7%, 9% and 42%.

2.4 Nitrogen analysis

A separate sample fragment (4.955 mg) was used for nitrogen analysis using a Noblesse HR (Nu Instruments) mass spectrometer with a dedicated nitrogen purification line. The sample was mounted in a windowed ultra-high vacuum laser chamber and gas was extracted via heating with a CO_2 laser. Three separate heating steps were performed with increasing laser power until the sample was completely fused. Nitrogen was purified using a CuO furnace following methods outlined in Boulliung et al. (2020). Additionally, neon and argon were measured using a separate aliquot of the extracted gas, following purification methods similar to those outlined in section 2.2. The three isotopologues of N_2 ($^{14}N^{14}N$, $^{15}N^{14}N$, $^{15}N^{15}N$) and the three isotopes of neon ($^{20,21,22}Ne$) and argon ($^{36,38,40}Ar$) were analyzed in multi-collection mode (Füri et al., 2021). Blank contributions for N_2 were <2% of measured signals, and standard reproducibility for $\delta^{15}N$ was 0.5‰.

3. Results

3.1 Step heating

Step heating isotope and abundance data for He, Ne and Ar were reported in Barrat et al., 2021, although as they are relevant to the following discussion they are reproduced for reference in Tables S1 & S2, and plotted in Fig. 1. The heavy noble gases Kr and Xe were indistinguishable from blank levels at the 600°C and 1000°C heating steps. while small but resolvable amounts were detected at the 800°C, 1200°C and 1400°C steps. Bulk ^{84}Kr and ^{132}Xe abundances are 160.8 ± 3.1 x10^{-16} mol.g^{-1} and 23.1 ± 1.6 x10^{-16} mol.g^{-1} respectively. Xe isotope spectra show strong enrichments in cosmogenic ^{124}Xe and ^{126}Xe, up to five times the atmospheric value (Fig. 3). Kr isotope spectra also show cosmogenic enrichments in light isotopes, particularly at the 1200°C extraction step

with $^{78}Kr/^{84}Kr$ ~2.5x the atmospheric value (Fig. 4). Excesses of ^{134}Xe and ^{136}Xe were observed, which will be described in section 4.1.3.

3.2 Crushing

Crushing data for light noble gases released at each of the 4 crushing steps are shown in Fig. 5 and reported in Tables 1 & 2. The largest release of gas was recorded in crushing step 2. The noble gas isotope compositions released during each crushing step are constrained to relatively narrow ranges, unlike step heating. This extraction technique is mechanical in nature and so not affected by thermal diffusion or mineral degradation.

The observed isotope ratios of the gas released during crushing are closer to terrestrial atmosphere values than those released during step heating, which may reflect a proportionally greater contribution of adsorbed atmosphere. Nonetheless, $^{3}He/^{4}He$ ratios up to 0.00342 ± 0.00006 are indicative of strong cosmogenic ^{3}He contributions, with a bulk value of 0.00331 ± 0.00006. Similarly, Ne isotopes are similar to expected cosmogenic production ratios, with a bulk $^{20}Ne/^{22}Ne$ of 0.866 ± 0.007 and $^{21}Ne/^{22}Ne$ of 0.692 ± 0.009. Fig. 2 shows that these ratios fall closer to expected cosmogenic production in a pure plagioclase phase than to the bulk composition, suggesting that the crushing is preferentially releasing plagioclase-hosted noble gases. Ar isotopes are again enriched in radiogenic ^{40}Ar and cosmogenic ^{38}Ar, with bulk $^{40}Ar/^{36}Ar$ and $^{38}Ar/^{36}Ar$ values of 3221 ± 57 and 0.413 ± 0.009, respectively. This lower $^{38}Ar/^{36}Ar$ value when compared to the bulk stepped heating data suggests a lower cosmogenic contribution, which may be a result of differential siting of cosmogenic and non-cosmogenic isotopes within the sample, or a higher atmospheric contribution in the crushed sample measurement. Total abundances of released ^{3}He, ^{20}Ne and ^{40}Ar during all crushing steps are 0.310 ± 0.015 $x10^{-13}$ $mol.g^{-1}$, 0.04854 ± 0.00064 $x10^{-13}$ $mol.g^{-1}$, and 0.2344 ± 0.0011 $mol.g^{-1}$ respectively.

Resolvable amounts of Kr and Xe were released only during crushing steps 1 and 2, with total ^{84}Kr and ^{132}Xe released equal to 2.59 ± 0.07 $x10^{-16}$ $mol.g^{-1}$ and 0.138 ± 0.034 $x10^{-16}$ $mol.g^{-1}$, respectively. Xe isotope spectra (shown in Fig. 3) are notably distinct from step heating results: no significant enrichments in cosmogenic isotopes are observed, but measurable excesses of fissiogenic isotopes ^{134}Xe and ^{136}Xe are present. This clearly indicates a difference in how cosmogenic and fissiogenic Xe isotopes are produced and stored within the sample. Whilst cosmogenic Xe isotopes are produced (and tightly retained) within the mineral lattice, Xe produced during spontaneous fission events can be ejected into surrounding inclusions and grain boundaries and reside there (Hebeda et al., 1987). Kr isotope spectra for crushing steps, shown in Fig. 4, display small but resolvable excesses in cosmogenic light isotopes, but no evidence for fissiogenic Kr contribution.

3.3 Laser Ablation

Abundance and isotope ratio data for the 6 laser ablation analyses are presented in Fig. 6 and Tables 1 & 2. The dramatic contrast between these analyses reveals a strong heterogeneity in noble gas signatures between the different mineral phases, Px and Pl. Pyroxenes have high abundances of ^{3}He and ^{20}Ne compared to the bulk sample, with ^{3}He ranging from 510 to 553 ($x10^{-13}$) $mol.cm^{-3}$ and ^{21}Ne from 101 to 109 ($x10^{-13}$) $mol.cm^{-3}$.

Assuming a mineral density of 3.4 g.cm^{-3}, this corresponds to approximately 1.5x enrichment in ^{3}He and 2x enrichment in ^{20}Ne compared to the bulk rock concentration. Conversely, ^{40}Ar abundances, while highly variable and ranging from 9 to 259 (x10^{-10}) mol.cm^{-3}, are consistently lower in Px1-5 than the bulk sample. ^{3}He/^{4}He ratios range from 0.00325 to 0.00647. Ne isotopes are mostly within the range of expected cosmogenic production ratios, as shown in Figure 2. ^{20}Ne/^{22}Ne ranges from 0.71 to 1.56, with this highest value suggesting a small trapped contribution, and ^{21}Ne/^{22}Ne ranges from 0.77 to 0.99. ^{40}Ar/^{36}Ar ratios range from 260 to 811, consistently lower than bulk values, whilst ^{38}Ar/^{36}Ar is highly variable between pyroxene grains, ranging from 0.42 up to 4.55, which is higher indeed than can be likely ascribed to bulk cosmogenic isotope production, and may reflect some small-scale heterogeneity revealed by laser ablation analyses. It should also be noted however, the large uncertainty associated with this high value, reflecting the extremely low quantity of gas released.

Analysis Plag1, targeting feldspar grains, shows contrasted signatures to the pyroxene analyses. He and Ne are both strongly depleted: ^{3}He abundance is 7 ± 1 x10^{-13} mol.cm^{-3} and ^{21}Ne was just 10 ± 0.4 x10^{-13} mol.cm^{-3} compared to values of >100 mol.cm^{-3} for the px analyses. Blank contributions to ^{20}Ne and ^{22}Ne precluded accurate determination of Ne isotope ratios, but ^{40}Ar is strongly enriched at 833 ± 94 x10^{-10} mol.cm^{-3}. This ^{40}Ar enrichment is further evidenced in the highest ^{40}Ar/^{36}Ar measured in this sample, at 50,400 ± 3700, with ^{38}Ar/^{36}Ar = 1.3 ± 0.1. Taken together, these laser ablation results show that cosmogenic He and Ne are strongly concentrated in individual pyroxene grains, whilst radiogenic ^{40}Ar is conversely concentrated in the interstitial plagioclase feldspar. The former of these observations may be due to the finer grained groundmass being unable to effectively retain the products of cosmic ray spallation, particularly for the lighter elements. The latter is intuitively the result of the greatly increased K abundance in the plagioclase. Nicklas et al. (2022) report an average K_2O content in the plagioclase phases of EC002 of 0.82 wt%, with undetectable quantities in the majority of their pyroxene analyses).

3.4 Nitrogen

Nitrogen isotopic and abundance data, as well as simultaneously acquired neon and argon data are presented in Table 5. The nitrogen isotopic ratio released in the first laser heating step is close to atmosphere, with δ^{15}N = 0.9 ± 0.5 ‰, and may reflect a contribution of surficial atmospheric contamination. However the two subsequent releases show clear enrichments in ^{15}N, with δ^{15}N values of 5.5 ± 0.5 ‰ and 45.0 ± 0.6 ‰ respectively. Bulk EC 002 δ^{15}N is 15.0 ± 0.5 ‰, rising to 20.7 ± 0.5 ‰ if the first step is discounted. Bulk N abundance is 3.82 ± 0.08 x10^{-7} mol.g^{-1}, equivalent to 5.3 ppm. Associated neon and argon data are similar to the bulk values obtained by step heating, with bulk ^{20}Ne/^{22}Ne = 0.802 ± 0.044, ^{21}Ne/^{22}Ne = 0.866 ± 0.077, ^{40}Ar/^{36}Ar = 9088 ± 251 and ^{38}Ar/^{36}Ar = 1.50 ± 0.04. A similar noble gas distribution is observed in the stepped laser extraction as in the step heating furnace extraction, with higher ^{40}Ar/^{36}Ar being released at lower temperatures. Neon isotopes are plotted in Fig. 2 where it can be seen that the first extraction step yields isotope ratios consistent with cosmogenic production from a plagioclase composition, whilst the latter two extraction steps are similar to cosmogenic production from a pyroxene composition. Abundances of ^{40}Ar and ^{21}Ne are also similar

to those observed in the step heating analysis, with ^{40}Ar abundance of 83.8 ± 2.0 x10^{-10} mol.g^{-1} and ^{21}Ne abundance of 20.3 ± 1.6 x10^{-13} mol.g^{-1}.

4. Discussion

4.1 Retention of noble gases produced by radioactive decay

4.1.1 Helium

^{4}He is produced directly as α-particles during decay of U-Th series nuclides. However, the produced ^{4}He has a low propensity to be effectively retained in most mineral structures due to its small atomic radius, high diffusivity, and the α-recoil imparted to the atom upon production. He is therefore only effectively retained in certain minerals (e.g. zircon and magnetite) and at low temperatures <200°C (Damon, 1957; Zeitler et al., 1987). A (U-Th)/He date can be calculated following Farley (2002):

$$^4He = 8 \times {}^{238}U(e^{\lambda_{238}t} - 1) + 7 \times {}^{235}U(e^{\lambda_{235}t} - 1) + 6 \times {}^{232}Th(e^{\lambda_{232}t} - 1) \quad (1)$$

Bulk U abundance in EC 002 is reported by Barrat et al. (2021) as 109 ppb. However, U abundance measurements are prone to alteration by terrestrial weathering, which is especially prevalent for desert finds such as EC 002 (e.g. Dreibus et al., 2007). We therefore estimate the pre-terrestrial U abundance indirectly using the bulk Th abundance of 136 ppb (Barrat et al., 2021) and divide by the chondritic Th/U ratio of 3.7, to obtain an estimate of 37 ppb U.

Assuming terrestrial U isotope ratio and correcting the ^{4}He abundance for cosmogenic ^{4}He assuming a cosmogenic production ratio ^{3}He/^{4}He of 0.2, this results in a calculated (U-Th)/He age of 2700 Myr. This age is far short of the ^{26}Al-^{26}Mg crystallization age of the sample (4565 Myr), indicating the loss of radiogenic He either partially or completely from some minerals.

4.1.2 Argon

^{40}Ar is produced as a result of ^{40}K decay, allowing ages to be calculated using the widely applied K-Ar system (Kelley, 2002). Whilst there are a number of complicating factors that make the determination of a reliable K-Ar age difficult for samples such as this one (Bogard, 2011), we can make a rough estimate of the time required to produce the observed levels of radiogenic ^{40}Ar. Using the bulk K abundance of 3057 ppm (Barrat et al., 2021) and assuming a terrestrial K isotopic composition results in a calculated K-Ar model age of 4530^{+120}_{-130} Myr. No correction for trapped ^{40}Ar is applied, as even if all trapped ^{36}Ar is atmospheric it would affect the resultant calculation by only 20 Myr. This is within error of the reported ^{26}Al-^{26}Mg age, and indicates that radiogenic ^{40}Ar has been effectively retained within Erg Chech 002 since shortly after its formation. As Ar is susceptible to escape via thermal diffusion from feldspar at temperatures above ~200°C (Cassata and Renne, 2013), we can thus ascertain that the sample has undergone no significant thermal events since shortly after its formation and the destruction of its original parent body.

4.1.3 Xenon

Xenon isotopes $^{131, 132, 134, 136}$Xe are produced in variable amounts by spontaneous fission of naturally occurring ^{238}U ($T_{1/2}$ = 4468 Myr). Additionally, in ancient samples, fissiogenic remnants of extinct ^{244}Pu ($T_{1/2}$ = 80 Myr) may be observed (Hudson et al., 1987). As the spontaneous fission of U and Pu produces these heavy Xe isotopes in characteristic proportions, the fissiogenic excesses can be used to identify the relative contributions of ^{238}U and ^{244}Pu to fissiogenic Xe (e.g. Parai and Mukhopadhyay, 2015). This can be calculated by comparing the ratios of the radiogenic excesses of these isotopes, normalised to ^{136}Xe.

$$^{136}Xe^{*} = {}^{136}Xe_{sample} - {}^{130}Xe_{sample} \times \left(\frac{^{136}Xe}{^{130}Xe}\right)_{air} \quad (2)$$

$$\frac{^{i}Xe^{*}}{^{136}Xe^{*}} = \frac{\frac{\left(\frac{^{i}Xe}{^{130}Xe}\right)_{sample}}{\left(\frac{^{i}Xe}{^{130}Xe}\right)_{air}} - 1}{\frac{\left(\frac{^{136}Xe}{^{130}Xe}\right)_{sample}}{\left(\frac{^{136}Xe}{^{130}Xe}\right)_{air}} - 1} \quad (3)$$

The resulting fissiogenic excess ratios are plotted in Fig. 7, alongside expected U and Pu fission yields (compiled from Ballentine and Burnard, 2002). The relatively large uncertainties associated with our data preclude a definitive assessment of the parent of the fissiogenic Xe, although the consistently low ^{132}Xe*/^{136}Xe* across our three measurements would favour U as the primary source (Fig. 7).

Given the age of EC 002 this is an unexpected result, as there would still have been significant extant ^{244}Pu present at the time of formation. In a closed system, Xe sourced from Pu fission is expected to dominate due to the greater spontaneous fission decay rate of ^{244}Pu compared to ^{238}U (Kuroda and Myers, 1994). This effect is readily seen in undegassed mantle samples from the (comparatively younger) Earth (Kunz et al., 1998; Mukhopadhyay, 2012).

The expected contribution of fissiogenic ^{136}Xe* produced over the lifetime of the sample can be calculated from the respective decay constants and fission yields (e.g. Ozima and Podosek, 2002). We use a sample U abundance of 37 ppb (see section 4.2.1) and assume a chondritic Pu/U of 0.0068 (Hudson et al., 1987). These parameters give an expected ^{136}Xe* of 1.55 x 10^{-16} mol.g^{-1}, with ~97% sourced from ^{244}Pu fission. Measured ^{136}Xe abundance in EC 002 is 7.72 x10^{-16} mol.g^{-1}, however the primordial isotope ratios are within uncertainty of atmospheric values, suggesting a contribution from secondary atmospheric contamination. We can correct for this atmospheric contribution to isolate the fissiogenic ^{136}Xe component. We calculate a ^{136}Xe* abundance of just 4.75 x10^{-17} mol.g^{-1} using Eq. 2. The discrepancy between measured and predicted ^{136}Xe* is unlikely to be due

to loss of Xe, as the more mobile radiogenic ^{40}Ar appears to have been effectively retained within the sample, as demonstrated in the previous section. Whilst Xe could possibly be lost via fissiogenic recoil (Hebeda et al., 1987), recoil distances for Xe ions are only ~5 µm in rocks (Ziegler, 1980), making it unlikely that Xe could be lost quantitatively via this mechanism (Ragettli et al., 1994).

Another possibility is that the assumption for Pu/U ratio is invalid in this case. Lugmair & Marti (1977) proposed a Pu/U ratio of 0.004 based on the analysis of achondrite Angra Dos Reis (ADOR), suggesting that planetary differentiation might have fractionated the Pu/U ratio towards lower values than the one determined by Hudson et al (1987) for the Saint-Séverin chondrite. This lower value for Pu/U would result in a lower expected $^{136}Xe^*$ of 9.32 $x10^{-17}$ $mol.g^{-1}$, much closer to our observed value.

4.2 Cosmogenic noble gases and exposure ages

4.2.1 Cosmogenic production model and initial parameters

The unique chemical composition of EC 002 precludes the robust application of semi-empirical methods for CRE age investigation, which are based on the comparative analysis of a number of meteorites from the same group (e.g. Eugster and Michel, 1995). As such, we must use a purely theoretical model derived *a priori* from the physical interactions of high-energy particles with solid matter. A number of these models have been developed specifically for the investigation of cosmogenic nuclide production within extraterrestrial samples (e.g. Leya et al., 2000; Leya and Masarik, 2009). These models produce theoretical predictions of cosmogenic nuclide production rates and their variation with chemical composition of the target material, size of the parent body and shielding depth of the sample within it. The chemical composition of the sample is a variable input parameter, and as such these models can be applied to a meteorite of any composition, or even to specific mineral phases within a meteorite (Roth et al., 2016). We are however unable to account satisfactorily for the matrix effect, as this must be considered for different meteorite groups during the initial construction of the model. In the rest of this discussion, we use the Leya & Masarik, 2009 model for cosmogenic production in ordinary chondrites, as this is the closest available analogue for EC 002, especially given its likely origin from partial melting of a non-carbonaceous chondrite (Barrat et al., 2021).

The Leya & Masarik, 2009, model allows for the calculation of production rates for all relevant noble gas isotopes (^{3}He, ^{20}Ne ^{21}Ne, ^{22}Ne, ^{36}Ar, ^{38}Ar). As production rate is strongly dependent on shielding, the consideration of multiple isotopes is typically required in order to find a unique solution for cosmogenic isotope production rates used to derive cosmic-ray exposure ages. The production ratio of two isotopes (e.g. $^{22}Ne/^{21}Ne$, $^{3}He/^{21}Ne$) can be used as a shielding correction parameter by comparing the theoretical production ratio to the observed data in order to estimate the true shielding experienced by the sample (Wieler, 2002). The pre-impact meteoroid radius is also a required model input, in order to properly account for 4π exposure. Based on a recovered mass of 32 kg of material, we estimate a 20 cm pre-impact radius for EC 002, although we note that a slightly larger radius will not have a significant effect on the following discussion.

4.2.2 CRE age modelling with He and Ne

In Fig. 8, we plot the modelled ^{21}Ne production rate (P21) vs shielding depth in a 40 cm-diameter body, as well as predicted production ratios of ^{22}Ne/^{21}Ne and ^{3}He/^{21}Ne for a range of pertinent chemical compositions, including the bulk EC 002 composition (Barrat et al., 2021), the average pyroxene and plagioclase compositions (Nicklas et al., 2022), as well as the compositions of the individual pyroxene and plagioclase phases targeted in our laser ablation analyses determined via SEM. The range of expected ^{20}Ne/^{22}Ne and ^{21}Ne/^{22}Ne production ratios for bulk, average pyroxene, and average plagioclase compositions are also shown in Fig. 2 alongside our measured data from various extraction techniques.

Conventionally, the shielding depth of the sample can be estimated by matching the observed cosmogenic production ratios to the theoretical values at different shielding depths. However, an immediate issue arising from the comparison of these theoretical production rates with our measured data is that our bulk ^{22}Ne/^{21}Ne and ^{3}He/^{21}Ne measurements are significantly different from those predicted for the bulk composition by theory, regardless of shielding depth. In terms of neon isotope composition, our bulk measurement plots much closer to the cosmogenic production ratio expected from a pure pyroxene phase (seen in Fig. 2 and Fig. 8), suggesting that the pyroxene grains are contributing the vast majority of the observed cosmogenic Ne present in the sample. This is perhaps unsurprising given that laser ablation data show extremely low ^{21}Ne abundances in the plagioclase compared to the pyroxenes (Fig. 6), to the extent that reliable neon isotope ratios could not be determined in the plagioclase analysis. Alongside the discordant (U-Th)/He date described in section 5.1.1, which indicates significant He loss from the sample, we conclude that cosmogenic Ne is not quantitatively retained in the plagioclase phases, and likely diffuses out over relatively short timescales, even at low temperatures. As such, any Ne- or He-derived cosmic ray exposure (CRE) age for bulk EC 002 is unlikely to represent the true exposure duration. Even if it were possible to accurately determine the proportion of pyroxene in our (now destroyed) sample, an assumption that 100% of cosmogenic Ne is derived from these pyroxene phases is tenuous, as low temperature step-heating results suggest at least a small cosmogenic Ne contribution from the plagioclase phases as well (Fig. 2).

The laser ablation data from individual pyroxenes may offer a more promising opportunity for constraining CRE age. However, whilst ^{21}Ne abundances in these analyses are relatively precise and consistent across the 5 pyroxenes analysed (Fig. 6), the isotopic ratios have significant uncertainties that preclude a reliable estimation of the shielding depth (due to relatively greater blank contribution to ^{20}Ne and ^{22}Ne). The expected P21 for average pyroxene composition ranges from 7.6 to 11.1 ($x10^{-14}$) $mol.g^{-1}.Myr^{-1}$ for our given range of shielding depths, giving a CRE age range from 27.6 to 40.6 Myr for our pyroxene measurements (average ^{21}Ne abundance of 3.08 $x10^{-12}$ $mol.g^{-1}$).

4.2.3 CRE age modelling with Ar

Argon is less widely used than the lighter noble gases for cosmogenic exposure anlaysis (Ott, 2002). However, given the apparent issues with He and Ne diffusive loss from plagioclase phases described in the previous section, Ar may prove more robust in this particular case. The K-Ar age calculated in section 4.1.2 is

concordant with the ^{26}Al-^{26}Mg age, suggesting that Ar has been quantitatively retained within the sample over its lifetime.

The predicted P38 values for bulk EC 002 composition range from 3.7 to 5.8 (x10^{-14}) mol.g^{-1}.Myr^{-1}. The deconvolution of the Ar composition of the stepped heating sample is shown in Table 6, where the cosmogenic abundance $[^{38}Ar]_{cos}$ = 2.20 x10^{-12} mol.g^{-1}. This corresponds to a CRE age range from 37.9 to 59.5 Myr. This age range overlaps with that derived from ^{21}Ne in individual pyroxenes. Unfortunately $P38_{bulk}/P21_{px}$ shows little variation with shielding depth, and cannot be used to reliably constrain it. Further constraints on CRE age could potentially be implemented using individual mineral Ar isotope data, but the Ar results from laser ablation are quite variable (which may be due to a greater heterogeneity in target elements for Ar as compared to He and Ne) and have large associated uncertainties due to the small amounts of gas released (Table 1).

4.3 Planetary noble gases

As discussed in the previous sections, the vast majority of the light noble gases, He and Ne, present in EC 002 are either cosmogenic or radiogenic in origin. As such, constraining the abundance of any trapped primordial or "planetary" component is not straightforward. Neon isotopes are indistinguishable from pure cosmogenic values, suggesting the primordial component is negligible. Furthermore, primordial Kr and Xe ratios are atmospheric, suggesting that any indigenous primordial component is so small that it is indistinguishable from inevitable atmospheric contamination. Argon therefore represents the only element for which a primordial component can be quantified, and this component may provide a crucial insight into the volatile degassing history of EC 002 and, by extension, of its parent body.

The deconvolution of the Ar composition of EC002 for both the stepped heating and laser heating samples is shown in Table 6. We find $[^{36}Ar]_{tr}$ = 6.98 x10^{-13} mol.g^{-1}, in the stepped heating sample, and $[^{36}Ar]_{tr}$ = 1.19 x10^{-13} mol.g^{-1} for the laser heating sample. As these values represent only a small fraction of the total Ar in the sample, their associated uncertainties are relatively large, on the order of the uncertainty of the total [^{36}Ar] measurements of 5 x10^{-14} and 3 x10^{-14} respectively. This non-cosmogenic ^{36}Ar may derive from a true primordial component, atmospheric contamination, or a mixture of both. As such, it can be considered to represent only an upper limit for the trapped ^{36}Ar abundance. However, the distinct nitrogen isotope ratio between EC 002 and the terrestrial atmosphere (+15.0 ‰) as well as the drastically different $^{36}Ar_{tr}$/N ratio (3.12 x10^{-7} compared to a terrestrial value of 2.01 x10^{-3}) are both evidence that atmospheric contamination is likely minimal.

This trapped ^{36}Ar abundance ($^{36}Ar_{tr}$) is within the range reported for other achondritic meteorites (Busemann and Eugster, 2002), although those values can vary greatly between different achondrite classes, and it is not clear which would represent the most suitable analogue. The $^{36}Ar_{tr}$ abundance of EC 002 is additionally around an order of magnitude lower than previously measured values for OC chondrites (e.g. Schelhaas et al., 1990), the likely parent composition from which the EC 002 melt was derived, indicating a significant extent of degassing.

The solubility of noble gases in a melt of andesitic composition was determined empirically by Lux, 1987, who reported a value for Ar of 6.9 x10^{-9} mol.g^{-1}.atm^{-1}. Using this value alongside our calculated primordial abundance, we can estimate the partial pressure of ^{36}Ar in equilibrium with EC 002 to be ~2 x10^{-5} atm. The physical interpretation of this value depends on whether EC 002 represents an extrusive or intrusive melt. This is comparable to the terrestrial atmospheric value of 3.1 x10^{-5} atm, and raises the possibility that the EC 002 parent body, and perhaps other early-forming planetesimals, could have possessed a relatively dense atmosphere during the earliest stages of solar system evolution.

4.4 Nitrogen and degassing history

The degassing history of EC 002 can also be investigated by looking at its nitrogen composition. Figure 9 shows the nitrogen isotopic composition and $^{36}Ar_{tr}$/N of EC 002 alongside literature data for selected meteorite groups. EC 002 is thought to have derived from melting of a precursor body with non-carbonaceous chondrite composition (Barrat et al., 2021). Figure 9 shows that EC 002 has δ^{15}N values within the range observed for pristine ordinary chondrites of petrographic type 3, but with a somewhat lower $^{36}Ar_{tr}$/N ratio.

$^{36}Ar_{tr}$/N may be fractionated during degassing from molten silicates, either during planetary differentiation or a magma ocean stage of accretion (Miyazaki et al., 2004). The degree of $^{36}Ar_{tr}$/N fractionation is highly dependent on the redox state of the molten silicate phase during degassing. Whilst Ar and N have similar solubility in silicate melts at and above the iron-wüstite (IW) buffer (Libourel et al., 2003; Miyazaki et al., 2004), N becomes much more soluble at more reducing conditions as it is able to form chemical bonds to H or Si, rather than remaining as inert N_2 (Boulliung et al., 2020). Furthermore, at these reduced conditions N isotopes may fractionate during degassing, with experimental evidence suggesting a possible fractionation factor of up to α_N = 1.035 (Dalou et al., 2022).

We apply a simple Rayleigh fractionation model to investigate degassing of EC 002 using the following equations to describe elemental ^{36}Ar/N and isotopic δ^{15}N fractionation respectively.

$$\left(\frac{^{36}Ar}{N}\right)_{init} = \frac{\left(\frac{^{36}Ar}{N}\right)_{obs}}{f^{(\alpha_{N-Ar}-1)}} \quad (4)$$

$$\delta^{15}N_{init} = \delta^{15}N_{obs} - (f-1) \times 1000 \ln(\alpha_N) \quad (5)$$

Where *f* is the fraction of N remaining in the melt, α_N is the isotopic fractionation factor for nitrogen degassing, and $\alpha_{N\text{-}Ar}$ is the elemental fractionation factor controlling ^{36}Ar/N (effectively the ratio of Ar to N solubility in silicate melt). The subscripts *obs* and *init* refer to the observed value (measured in our sample) and the hypothetical initial value of the EC 002 parent body prior to degassing. This formulation explicitly solves for the initial composition, as our observed value represents the composition after a certain level of degassing *f*.

As such, we calculate here the range of initial compositions from which it is possible to produce the EC 002 composition by degassing.

We consider two degassing scenarios, representing degassing at low pressure under oxidised and reduced conditions respectively. For oxidising conditions we assume negligble isotopic fractionation (Cartigny et al., 2001), and N solubility twice that of Ar ($\alpha_N = 1$; $\alpha_{N\text{-}Ar} = 2$). Under reducing conditions we assume isotopic fractionation similar to that observed by Dalou et al., 2022, consistent with kinetic degassing of N primarily speciated as NH_3, and N solubility 10x higher than Ar ($\alpha_N = 1.035$; $\alpha_{N\text{-}Ar} = 10$). For each of these scenarios we calculate the range of possible starting compositions considering that EC 002 represents the degassed composition with *f* representing the fraction of degassing experienced. The resulting composition curves are plotted in Fig. 9, labeled (ox) and (red) respectively, with annotations showing the level of degassing that would have been experienced from given starting compositions.

Both the oxidising and reducing models are clearly compatible with EC 002 being derived from an OC-like parent body, but the level of degassing required is markedly different between the two scenarios. Under oxidising conditions, >80% degassing is required for the initial composition to be within the observed OC range, whilst under reducing conditions only around 20-40% degassing is required. Crucially however the degassing model is incompatible with a parent body composition of the other major class of non-carbonaceous chondrites, the enstatite chondrites (typically abbreviated as EC although EnCh is used henceforth to avoid confusion with the unrelated EC 002). This refinement of the possible parent body composition from non-carbonaceous (EnCh + OC) down to OC is important for understanding the origin of the EC 002 parent body as EnCh are thought to have formed closer to the sun (e.g. Piani et al., 2020). Furthermore, Earth displays nucleosynthetic isotope signatures primarily favouring an EnCh-like origin (Carlson et al., 2018), and so this may preclude a genetic link between Earth and the EC 002 parent body.

5. Conclusion

Erg Chech 002 is a unique meteorite that expands our understanding of the range of geological processes occurring in the early solar system. We present a comprehensive analysis of its noble gas composition, using a variety of extraction techniques to fully characterise the distribution of noble gas components within different phases.

Combined step heating and laser ablation analyses demonstrate a clear dichotomy between the pyroxene and plagioclase phases of EC 002 in terms of their ability to retain noble gases of cosmogenic and radiogenic origin. He and Ne appear to be quantitatively lost from the plagioclase phases, resulting in inconsistent cosmic ray exposure ages and radiogenic (U-Th)/He age. He and Ne laser ablation analysis shows that there is significant preservation of cosmogenic isotopes within the pyroxene phases. Conversely, Ar appears to be effectively retained in both pyroxene and plagioclase phases, with coherent K-Ar age. Thus we consider Ar to be a more reliable candidate for cosmic ray exposure age, although the unreliability of He and Ne in this regard makes shielding corrections problematic. This comprehensive analysis of all noble gas isotopes across

different phases here demonstrates the potential pitfalls of relying solely on single noble gas element datasets for cosmogenic and radiogenic calculations.

Cosmogenic and radiogenic excesses are also observed in the heavy noble gases Kr and Xe. The levels of observed fissiogenic $^{136}Xe^*$ are slightly lower than would be expected for a sample of this age, and may indicate that the initial Pu/U of the EC 002 parent body was non-chondritic. As the noble gas inventory is dominated by radiogenic and cosmogenic isotopes, determination of primordial isotope abundances is not straightforward, although the non-cosmogenic ^{36}Ar abundances suggest that the sample is not completely degassed. Nitrogen isotope analysis and $^{36}Ar/N$ ratios support an OC-like initial volatile composition for the EC 002 parent body.

Acknowledgments: This study was supported by the European Research Council (ERC) under the European Union's Horizon 2020 research and innovation program (PHOTONIS Advanced Grant # 695618 to BM and VOLATILIS Starting Grant 715028 to EF).

References

Anand A., Kruttasch P. M. and Mezger K. (2022) 53Mn-53Cr chronology and ε54Cr-Δ17O genealogy of Erg Chech 002: The oldest andesite in the solar system. *Meteoritics & Planetary Science* **57**, 2003–2016.

Ballentine C. J. and Burnard P. G. (2002) Production, Release and Transport of Noble Gases in the Continental Crust. *Reviews in Mineralogy and Geochemistry* **47**, 481–538.

Barrat J.-A., Chaussidon M., Yamaguchi A., Beck P., Villeneuve J., Byrne D. J., Broadley M. W. and Marty B. (2021) A 4,565-My-old andesite from an extinct chondritic protoplanet. *PNAS* **118**.

Bekaert D. V., Broadley M. W., Delarue F., Avice G., Robert F. and Marty B. (2018) Archean kerogen as a new tracer of atmospheric evolution: Implications for dating the widespread nature of early life. *Science Advances* **4**, eaar2091.

Bekaert D. V., Curtice J., Meier M. M. M., Byrne D. J., Broadley M. W., Seltzer A., Barry P., Kurz M. D. and Nielsen S. G. (2022) Determining the noble gas cosmic ray exposure ages of 23 meteorites (8 chondrites and 15 achondrites) from modeling and empirical methods. *Meteoritics & Planetary Science* **57**, 1542–1569.

Bekaert D. V., Marrocchi Y., Meshik A., Remusat L. and Marty B. (2019) Primordial heavy noble gases in the pristine Paris carbonaceous chondrite. *Meteoritics & Planetary Science* **54**, 395–414.

Bogard D. D. (2011) K–Ar ages of meteorites: Clues to parent-body thermal histories. *Geochemistry* **71**, 207–226.

Boulliung J., Füri E., Dalou C., Tissandier L., Zimmermann L. and Marrocchi Y. (2020) Oxygen fugacity and melt composition controls on nitrogen solubility in silicate melts. *Geochimica et Cosmochimica Acta* **284**, 120–133.

Broadley M. W., Barry P. H., Bekaert D. V., Byrne D. J., Caracausi A., Ballentine C. J. and Marty B. (2020a) Identification of chondritic krypton and xenon in Yellowstone gases and the timing of terrestrial volatile accretion. *PNAS* **117**, 13997–14004.

Broadley M. W., Bekaert D. V., Marty B., Yamaguchi A. and Barrat J.-A. (2020b) Noble gas variations in ureilites and their implications for ureilite parent body formation. *Geochimica et Cosmochimica Acta* **270**, 325–337.

Busemann H. and Eugster O. (2002) The trapped noble gas component in achondrites. *Meteoritics & Planetary Science* **37**, 1865–1891.

Carlson R. W., Brasser R., Yin Q.-Z., Fischer-Gödde M. and Qin L. (2018) Feedstocks of the Terrestrial Planets. *Space Sci Rev* **214**, 121.

Cartigny P., Jendrzejewski N., Pineau F., Petit E. and Javoy M. (2001) Volatile (C, N, Ar) variability in MORB and the respective roles of mantle source heterogeneity and degassing: the case of the Southwest Indian Ridge. *Earth and Planetary Science Letters* **194**, 241–257.

Cassata W. S. and Renne P. R. (2013) Systematic variations of argon diffusion in feldspars and implications for thermochronometry. *Geochimica et Cosmochimica Acta* **112**, 251–287.

Chaussidon M., Barrat J. A., Yamaguchi A., Beck P., Villeneuve J., Byrne D. J., Broadleye M. W. and Marty B. (2021) 26Al Chronology of Erg Chech 002, the Oldest Andesite in the Solar System. In Lunar and Planetary Science Conference. p. 2222.

Dai W., Moynier F., Fang L. and Siebert J. (2023) K-Ca dating and Ca isotope composition of the oldest Solar System lava, Erg Chech 002. *Geochem. Persp. Let.* **24**, 33–37.

Dalou C., Deligny C. and Füri E. (2022) Nitrogen isotope fractionation during magma ocean degassing: tracing the composition of early Earth's atmosphere. *Geochem. Persp. Let.*, 27–31.

Damon P. E. (1957) Determination of radiogenic helium in zircon by stable isotope dilution technique. *Trans. AGU* **38**, 945.

Day J. M. D., Ash R. D., Liu Y., Bellucci J. J., Iii D. R., McDonough W. F., Walker R. J. and Taylor L. A. (2009) Early formation of evolved asteroidal crust. *Nature* **457**, 179–182.

Dreibus G., Haubold R., Huisl W. and SpetTEL B. (2007) Gain and loss of uranium by meteorites and rocks, and implications for the redistribution of uranium on Mars. *Meteoritics & Planetary Science* **42**, 951–962.

Eugster O. and Michel Th. (1995) Common asteroid break-up events of eucrites, diogenites, and howardites and cosmic-ray production rates for noble gases in achondrites. *Geochimica et Cosmochimica Acta* **59**, 177–199.

Fang L., Frossard P., Boyet M., Bouvier A., Barrat J.-A., Chaussidon M. and Moynier F. (2022) Half-life and initial Solar System abundance of 146Sm determined from the oldest andesitic meteorite. *Proc. Natl. Acad. Sci. U.S.A.* **119**.

Farley K. A. (2002) (U-Th)/He Dating: Techniques, Calibrations, and Applications. *Reviews in Mineralogy and Geochemistry* **47**, 819–844.

Füri E., Zimmermann L. and Hiesinger H. (2021) Noble gas exposure ages of samples from Cone and North Ray craters: Implications for the recent lunar cratering chronology. *Meteoritics & Planetary Science* **56**, 2047–2061.

583 Grady M. M., Verchovsky A. B., Franchi I. A., Wright I. P. and Pillinger C. T. (2002) Light dement
584 geochemistry of the Tagish Lake CI2 chondrite: Comparison with CI1 and CM2 meteorites.
585 *Meteoritics & Planetary Science* **37**, 713–735.

586 Hashizume K. and Sugiura N. (1995) Nitrogen isotopes in bulk ordinary chondrites. *Geochimica et*
587 *Cosmochimica Acta* **59**, 4057–4069.

588 Hebeda E. H., Schultz L. and Freundel M. (1987) Radiogenic, fissiogenic and nucleogenic noble gases
589 in zircons. *Earth and Planetary Science Letters* **85**, 79–90.

590 Hudson G. B., Kennedy B. M., Podosek F. A. and Hohenberg C. M. (1987) *The early solar system*
591 *abundance of 244Pu as inferred from the St Severin chondrite*., United States.

592 Kelley S. (2002) K-Ar and Ar-Ar Dating. *Reviews in Mineralogy and Geochemistry* **47**, 785–818.

593 Kerridge J. F. (1985) Carbon, hydrogen and nitrogen in carbonaceous chondrites: Abundances and
594 isotopic compositions in bulk samples. *Geochimica et Cosmochimica Acta* **49**, 1707–1714.

595 Kruijer T. S., Touboul M., Fischer-Gödde M., Bermingham K. R., Walker R. J. and Kleine T. (2014)
596 Protracted core formation and rapid accretion of protoplanets. *Science*.

597 Kunz J., Staudacher T. and Allègre C. J. (1998) Plutonium-Fission Xenon Found in Earth's Mantle.
598 *Science* **280**, 877–880.

599 Kuroda P. K. and Myers W. A. (1994) Plutonium-244 Fission Xenon in the Most Primitive Meteorites.
600 *Radiochimica Acta* **64**, 167–174.

601 Leya I., Ammon K., Cosarinsky M., Dalcher N., Gnos E., Hofmann B. and Huber L. (2013) Light noble
602 gases in 12 meteorites from the Omani desert, Australia, Mauritania, Canada, and Sweden.
603 *Meteoritics & Planetary Science* **48**, 1401–1414.

604 Leya I., Lange H.-J., Neumann S., Wieler R. and Michel R. (2000) The production of cosmogenic
605 nuclides in stony meteoroids by galactic cosmic-ray particles. *Meteoritics & Planetary*
606 *Science* **35**, 259–286.

607 Leya I. and Masarik J. (2009) Cosmogenic nuclides in stony meteorites revisited. *Meteoritics &*
608 *Planetary Science* **44**, 1061–1086.

609 Libourel G., Marty B. and Humbert F. (2003) Nitrogen solubility in basaltic melt. Part I. Effect of
610 oxygen fugacity. *Geochimica et Cosmochimica Acta* **67**, 4123–4135.

611 Lugmair G. W. and Marti K. (1977) SmNdPu timepieces in the Angra dos Reis meteorite. *Earth and*
612 *Planetary Science Letters* **35**, 273–284.

613 Mahajan R. R., Sarbadhikari A. B. and Sisodia M. S. (2019) Noble gas, nitrogen composition and
614 cosmic ray exposure history of two eucrites Vissannapeta, Piplia Kalan and one howardite
615 Lohawat. *Planetary and Space Science* **165**, 23–30.

616 Matsuda J., Matsumoto T., Sumino H., Nagao K., Yamamoto J., Miura Y., Kaneoka I., Takahata N. and
617 Sano Y. (2002) The 3He/4He ratio of the new internal He Standard of Japan (HESJ).
618 *Geochemical Journal* **36**, 191–195.

Mazor E., Heymann D. and Anders E. (1970) Noble gases in carbonaceous chondrites. *Geochimica et Cosmochimica Acta* **34**, 781–824.

Meier M. M. M., Bindi L., Heck P. R., Neander A. I., Spring N. H., Riebe M. E. I., Maden C., Baur H., Steinhardt P. J., Wieler R. and Busemann H. (2018) Cosmic history and a candidate parent asteroid for the quasicrystal-bearing meteorite Khatyrka. *Earth and Planetary Science Letters* **490**, 122–131.

Miyazaki A., Hiyagon H., Sugiura N., Hirose K. and Takahashi E. (2004) Solubilities of nitrogen and noble gases in silicate melts under various oxygen fugacities: implications for the origin and degassing history of nitrogen and noble gases in the earth. *Geochimica et Cosmochimica Acta* **68**, 387–401.

Mukhopadhyay S. (2012) Early differentiation and volatile accretion recorded in deep-mantle neon and xenon. *Nature* **486**, 101–104.

Nakamura T., Noguchi T., Zolensky M. E. and Tanaka M. (2003) Mineralogy and noble-gas signatures of the carbonate-rich lithology of the Tagish Lake carbonaceous chondrite: evidence for an accretionary breccia. *Earth and Planetary Science Letters* **207**, 83–101.

Nicklas R. W., Day J. M. D., Gardner-Vandy K. G. and Udry A. (2022) Early silicic magmatism on a differentiated asteroid. *Nat. Geosci.* **15**, 696–699.

Ozima M. and Podosek F. A. (2002) *Noble gas geochemistry*., Cambridge University Press.

Parai R. and Mukhopadhyay S. (2015) The evolution of MORB and plume mantle volatile budgets: Constraints from fission Xe isotopes in Southwest Indian Ridge basalts. *Geochemistry, Geophysics, Geosystems* **16**, 719–735.

Piani L., Marrocchi Y., Rigaudier T., Vacher L. G., Thomassin D. and Marty B. (2020) Earth's water may have been inherited from material similar to enstatite chondrite meteorites. *Science* **369**, 1110–1113.

Pravdivtseva O., Tissot F. L. H., Dauphas N. and Amari S. (2020) Evidence of presolar SiC in the Allende Curious Marie calcium–aluminium-rich inclusion. *Nat Astron*, 1–8.

Ragettli R. A., Hebeda E. H., Signer P. and Wieler R. (1994) Uranium-xenon chronology: precise determination of λsƒ ∗136Ysƒ for spontaneous fission of 238U. *Earth and Planetary Science Letters* **128**, 653–670.

Rai V. K, Murty S. V. S. and Ott U. (2003) Nitrogen components in ureilites. *Geochimica et Cosmochimica Acta* **67**, 2213–2237.

Rai V. K., Murty S. V. S. and Ott U. (2003) Noble gases in ureilites: cosmogenic, radiogenic, and trapped components. *Geochimica et Cosmochimica Acta* **67**, 4435–4456.

Riebe M. E. I., Huber L., Metzler K., Busemann H., Luginbuehl S. M., Meier M. M. M., Maden C. and Wieler R. (2017) Cosmogenic He and Ne in chondrules from clastic matrix and a lithic clast of Murchison: No pre-irradiation by the early sun. *Geochimica et Cosmochimica Acta* **213**, 618–634.

Roth A. S. G., Metzler K., Baumgartner L. P. and Leya I. (2016) Cosmic-ray exposure ages of chondrules. *Meteoritics & Planetary Science* **51**, 1256–1267.

Schelhaas N., Ott U. and Begemann F. (1990) Trapped noble gases in unequilibrated ordinary chondrites. *Geochimica et Cosmochimica Acta* **54**, 2869–2882.

Scherer P. and Schultz L. (2000) Noble gas record, collisional history, and pairing of CV, CO, CK, and other carbonaceous chondrites. *Meteoritics & Planetary Science* **35**, 145–153.

Spitzer F., Burkhardt C., Nimmo F. and Kleine T. (2021) Nucleosynthetic Pt isotope anomalies and the Hf-W chronology of core formation in inner and outer solar system planetesimals. *Earth and Planetary Science Letters* **576**, 117211.

Srinivasan P., Dunlap D. R., Agee C. B., Wadhwa M., Coleff D., Ziegler K., Zeigler R. and McCubbin F. M. (2018) Silica-rich volcanism in the early solar system dated at 4.565 Ga. *Nat Commun* **9**, 3036.

Takenouchi A., Sumino H., Yamaguchi A. and Barrat J. A. (2021) Noble Gas Chronology of Erg Chech 002 Ungrouped Achondrite. **84**, 6162.

Wieler R. (2002) Cosmic-Ray-Produced Noble Gases in Meteorites. *Reviews in Mineralogy and Geochemistry* **47**, 125–170.

Zeitler P. K., Herczeg A. L., McDougall I. and Honda M. (1987) U-Th-He dating of apatite: A potential thermochronometer. *Geochimica et Cosmochimica Acta* **51**, 2865–2868.

Ziegler J. F. (1980) Handbook of stopping cross-sections for energetic ions in all elements.

677 **Figures**

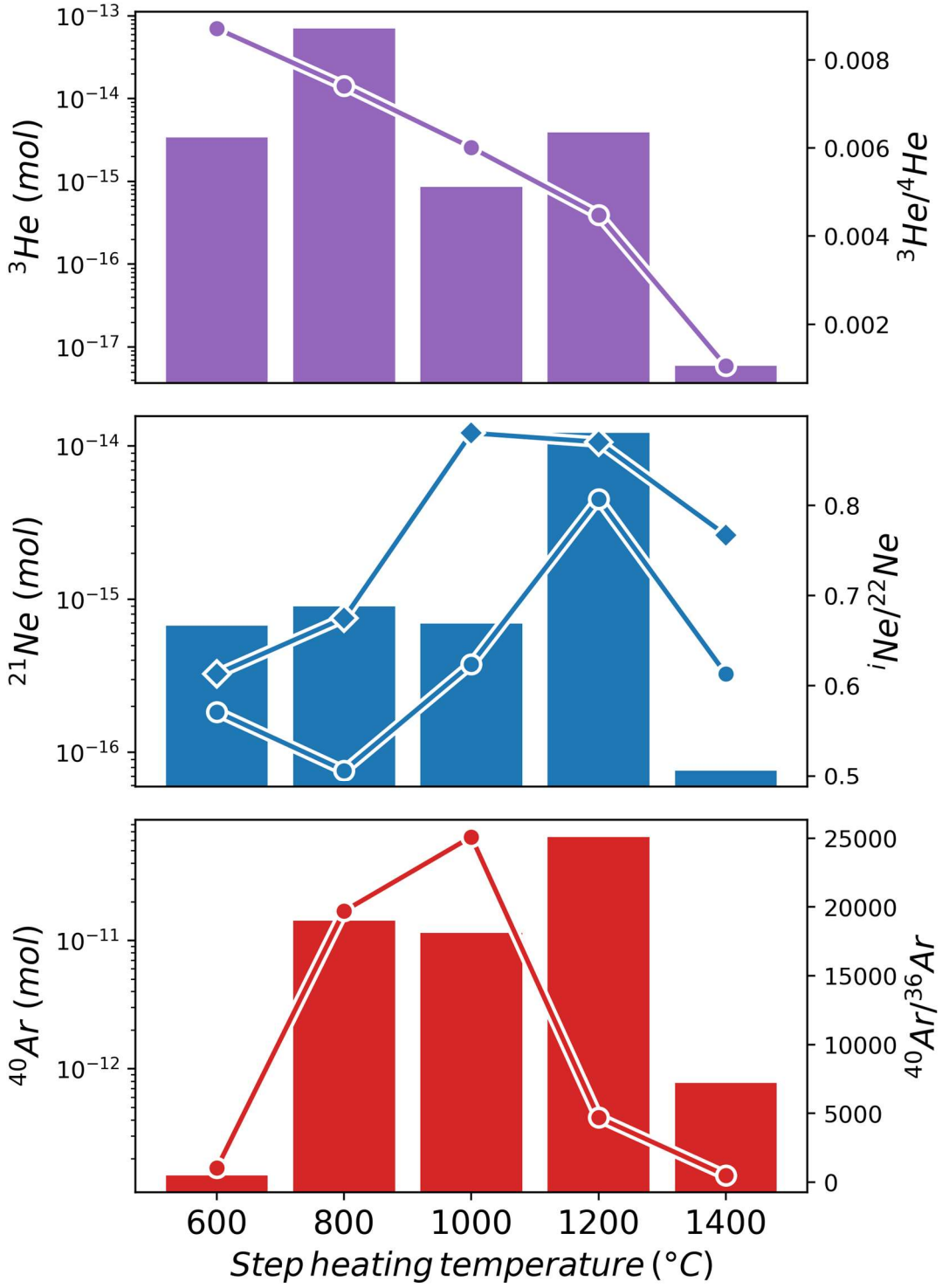

678

679 **Figure 1 -** Isotope and abundance data for light noble gases released by step heating extraction from 8.3 mg
680 sample. The amount of gas released at each step (in mol) is represented by bars, with values denoted on the
681 left-hand axis (log scale). Isotope ratios for the corresponding element are overlain as connected points, with
682 these values shown on the right hand axis. For neon, $^{21}Ne/^{22}Ne$ ratios are marked with diamonds, and

683 $^{20}Ne/^{22}Ne$ marked with circles. This shows that the majority of He was released during the 800°C heating step,
684 whereas Ne and Ar were mostly released at the 1200°C step.

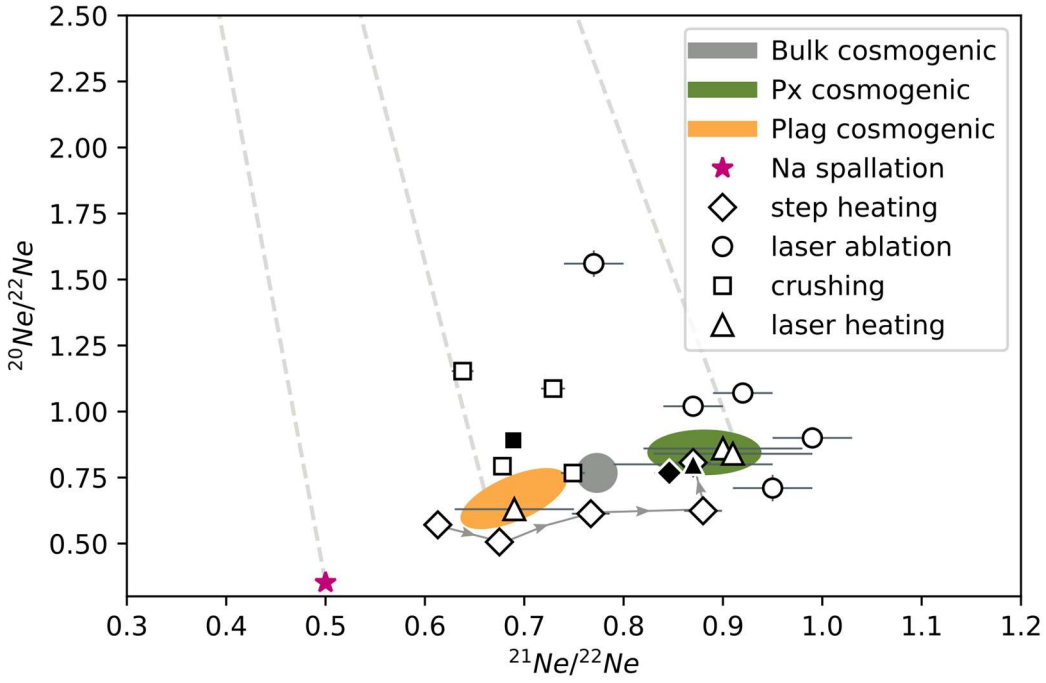

685

686 **Figure 2 -** Neon isotope plot for Erg Chech 002 data using different extraction methods. Step heating, laser
687 ablation, crushing and laser heating extractions are shown using diamond, circular, square and triangular
688 markers respectively. Individual measurements are shown as unfilled markers, and bulk extraction values for
689 step heating and crushing are shown as filled markers. All laser ablation analyses are from pyroxene grains as
690 insufficient neon was released from the plagioclase analysis. Approximate galactic cosmic ray production
691 endmembers are shown as shaded regions, determined over all shielding depths for a 20 cm radius asteroid
692 for the bulk, px and plag composition of EC 002 respectively, after Leya and Masarik, 2009. Grey dashed lines
693 show mixing with atmospheric neon. Other neon endmembers such as Ne-HL, Ne-B (implantation-fractionated
694 solar wind) and phase Q are in approximately the same direction as atmosphere at this scale. Lower
695 temperature heating steps plot towards the predicted production ratios of spallation on pure Na (Leya et al.,
696 2000; Pravdivtseva et al., 2020). This may be due to the preferential release of neon from Na-rich sodic
697 plagioclase phases at lower temperature steps. Conversely, laser ablation analyses, which were targeted
698 within individual pyroxene phenocrysts, show higher $^{21}Ne/^{22}Ne$ than predicted bulk production, falling closer
699 to expected production from pure pyroxene.

700

701

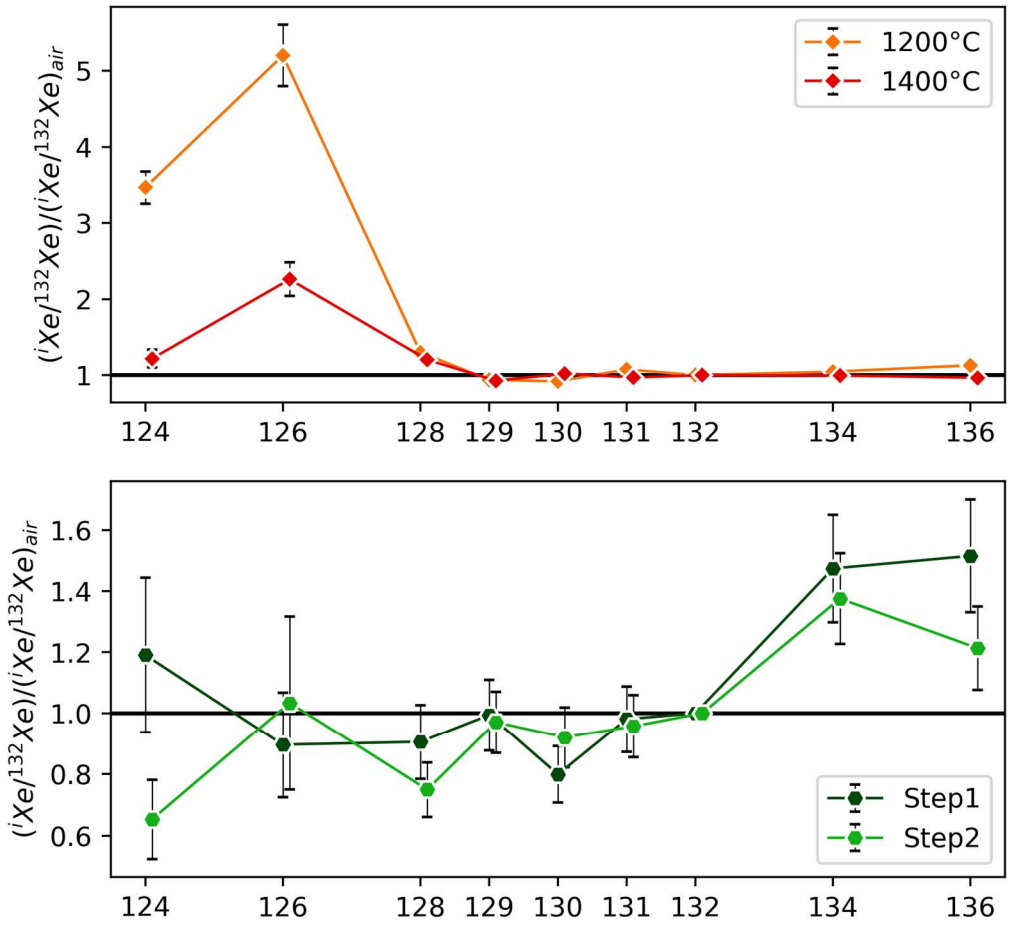

Figure 3 - Xe isotope spectra for Erg Chech 002 gas released during step heating (top panel) and crushing (bottom panel). Isotope mass number is shown along the x-axis; values on the y-axis are normalised to ^{132}Xe and then to the atmospheric ratio. Step heating extractions at 1200°C and 1400°C show strong enrichments in cosmogenic ^{124}Xe and ^{126}Xe. Crushing steps 1 and 2 both show resolvable excesses in fissiogenic isotopes ^{134}Xe and ^{136}Xe.

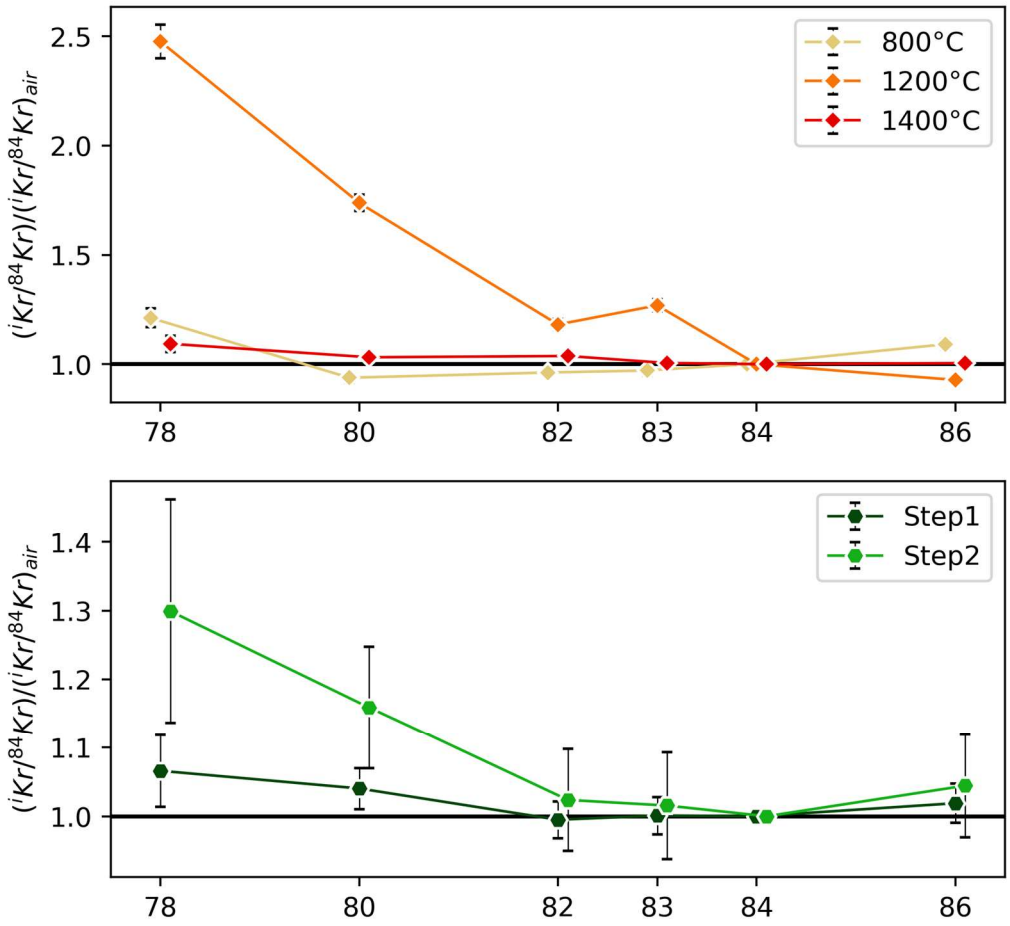

709

710 **Figure 4 -** Kr isotope spectra for Erg Chech 002 gas released during step heating (top panel) and crushing
711 (bottom panel). Isotope mass number is shown along the x-axis; values on the y-axis are normalised to ^{84}Kr and
712 then to the atmospheric ratio. Cosmogenic excesses of light Kr isotopes are clearly visible in both the step
713 heating and crushing results.

714

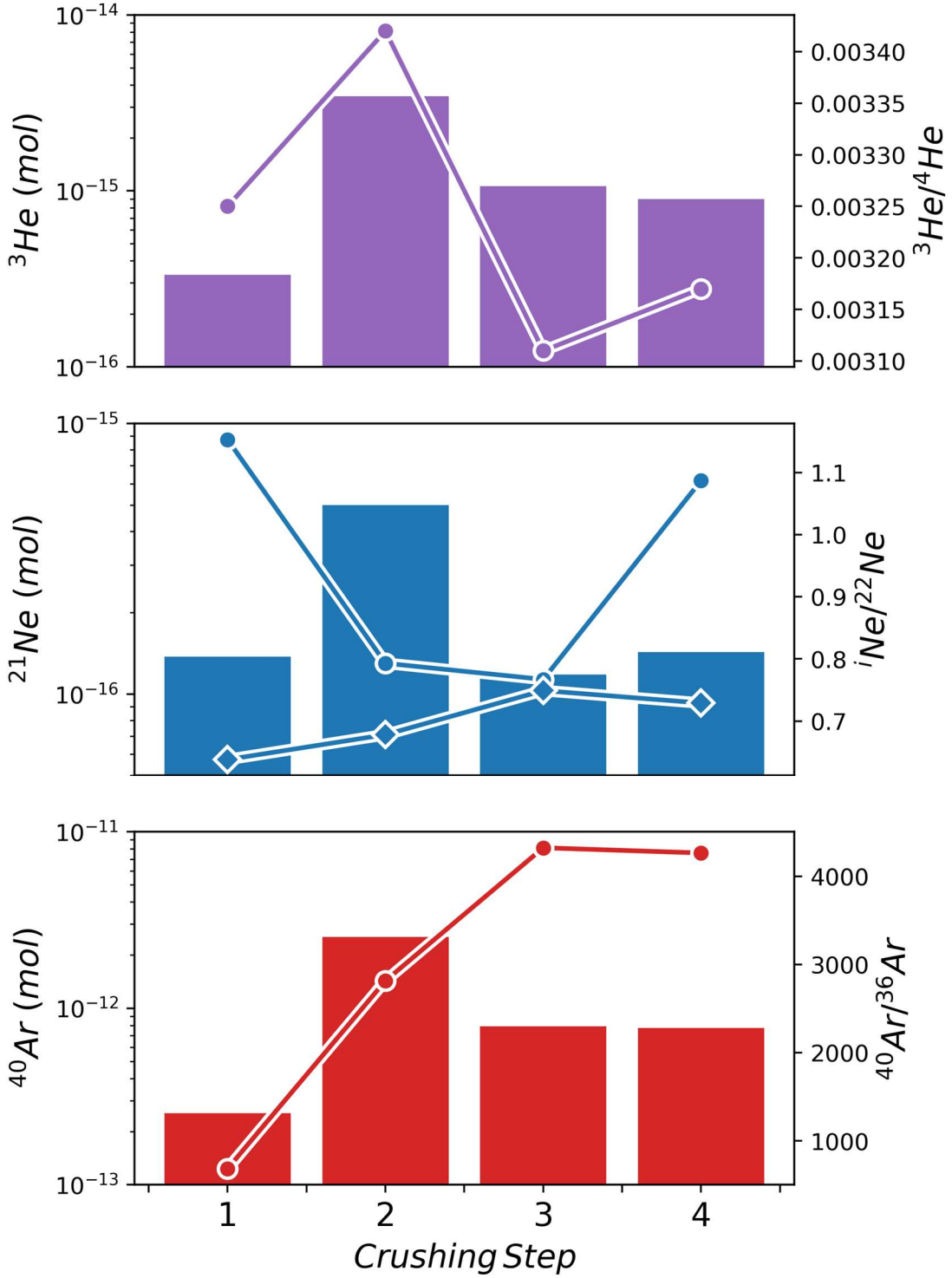

715

716 **Figure 5 -** Isotope and abundance data for light noble gases released by crushing. The amount of gas released
717 at each step (in mol) is represented by bars, with values denoted on the left hand axis (log scale). Isotope
718 ratios for the corresponding element are overlain as connected points, with these values shown on the right
719 hand axis. For neon, $^{21}Ne/^{22}Ne$ ratios are marked with diamonds, and $^{20}Ne/^{22}Ne$ marked with circles.

720

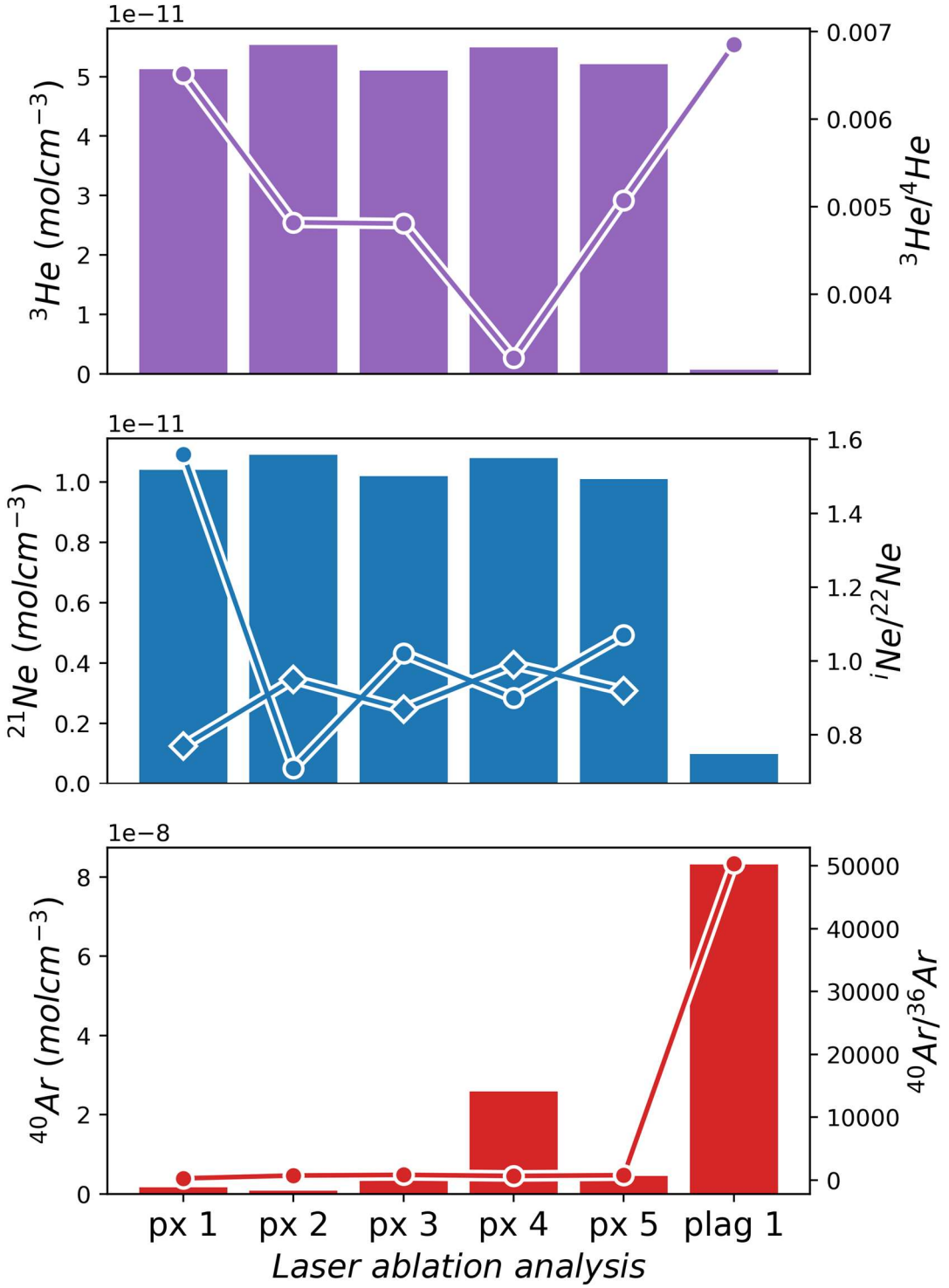

721

722 **Figure 6 -** Isotope and abundance data for laser ablation analyses. The isotope abundance for each analysis site
723 is represented as bars, with values denoted on the left hand axis (log scale). Isotope ratios for the
724 corresponding element are overlain as connected points, with these values shown on the right hand axis. For
725 neon, $^{21}Ne/^{22}Ne$ ratios are marked with diamonds, and $^{20}Ne/^{22}Ne$ marked with circles.

726

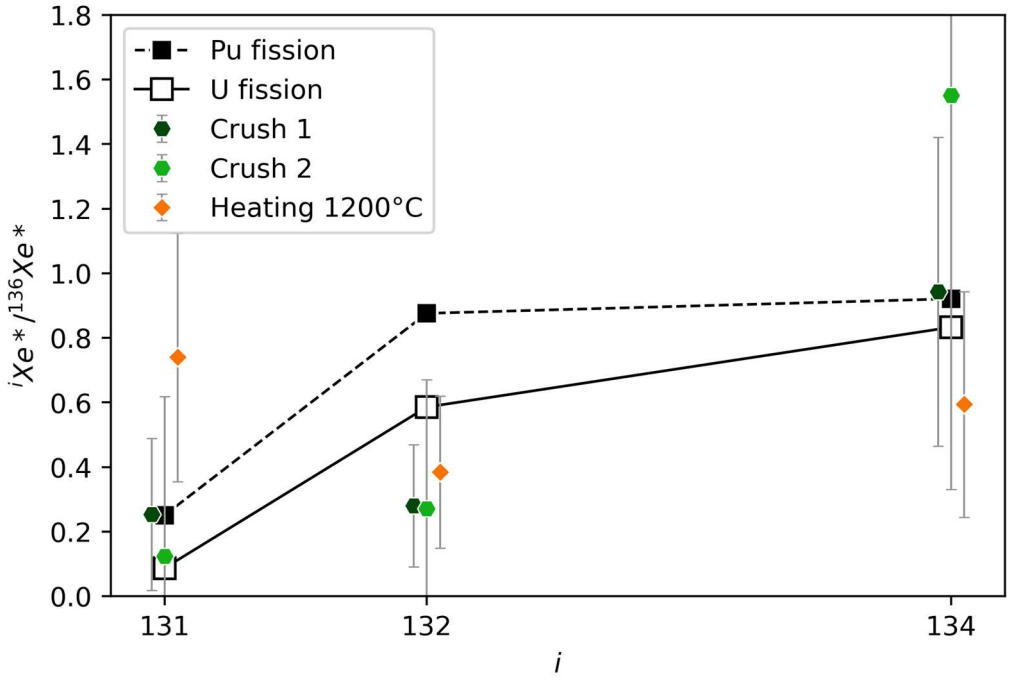

727

728 **Figure 7 -** Fissiogenic Xe isotope data for selected sample steps that show distinguishable excesses. Excesses of
729 each isotope are normalised to the observed excess of ^{136}Xe, and compared to the expected fissiogenic spectra
730 of U and Pu.

731

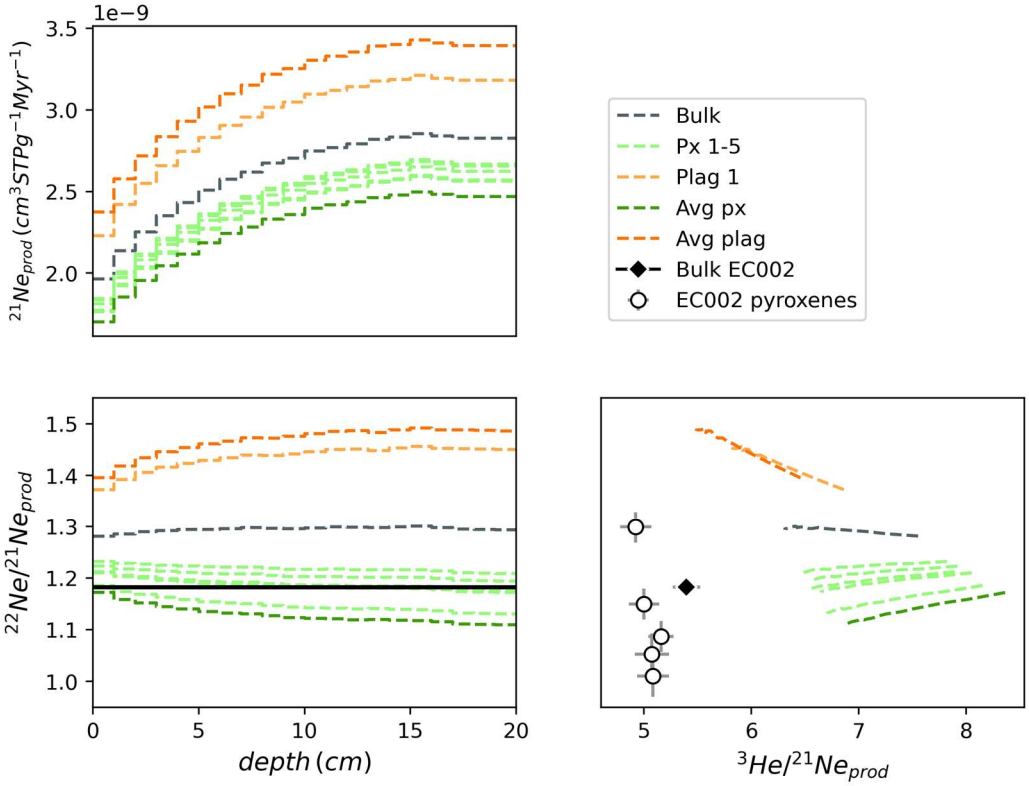

732

733 **Figure 8 -** Cosmogenic production rate models for EC 002 using bulk chemical composition, average pyroxene
734 and plagioclase compositions as measured by Nicklas et al., 2022, and individual pyroxene and plagioclase
735 compositions corresponding to our laser ablation analyses. Left hand panels show predicted ^{21}Ne and
736 ^{21}Ne/^{22}Ne production with increasing depth within a 20cm radius meteoroid, with bulk EC 002 ^{22}Ne/^{21}Ne
737 shown as a solid black line. Right hand panel shows predicted ^{22}Ne/^{21}Ne vs ^{3}He/^{21}Ne curves alongside bulk EC
738 002 composition and individual pyroxene compositions as measured by laser ablation.

739

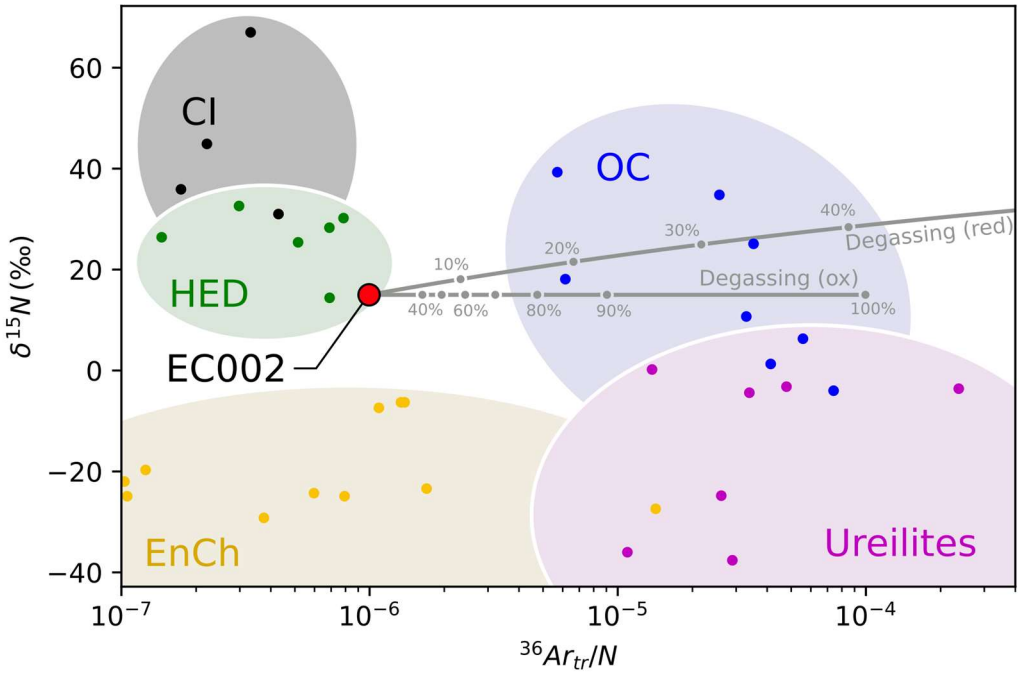

740

741 **Figure 9 -** Nitrogen isotope and $^{36}Ar_{tr}/N$ (^{36}Ar corrected for cosmogenic contribution) values for EC 002
742 alongside literature values for selected meteorite classes: CI-group carbonaceous chondrites (CI), enstatite
743 chondrites (EnCh), Howardite-Eucrite-Diogenites (HED), ordinary chondrites (OC), and Ureilites. All OC data
744 shown are from specimens of petrographic type 3, being the least altered. Data are compiled from (Mazor et
745 al., 1970; Kerridge, 1985; Hashizume and Sugiura, 1995; Grady et al., 2002; Nakamura et al., 2003; Rai et al.,
746 2003; Rai et al., 2003; Mahajan et al., 2019). Grey lines show ranges of possible parent body compositions
747 from which the EC 002 composition can be obtained by degassing under selected oxidising and reducing
748 conditions as outlined in section 4.4. Annotated percentages denote the level of degassing which would be
749 required for EC 002 having started from the relevant composition shown. Uncertainty for the EC 002 point is
750 within the marker size.

751 **Table 1 -** Light noble gas isotope ratios measured in Erg Chech 002 using step heating, crushing and laser ablation techniques. Laser ablation analyses Px1-5 targeted pyroxene
752 grains whilst Plag1 targeted the plagioclase phase. Uncertainties shown are at the 1σ level. Results for step heating are reported in Barrat et al., 2021, and reproduced in
753 Table S1 for reference.

754

	$^{3}He/^{4}He$	±	$^{20}Ne/^{22}Ne$	±	$^{21}Ne/^{22}Ne$	±	$^{40}Ar/^{36}Ar$	±	$^{38}Ar/^{36}Ar$	±
Crushing										
Step 1	0.00325	0.00008	1.153	0.015	0.638	0.011	686	6	0.232	0.005
Step 2	0.00342	0.00006	0.793	0.006	0.678	0.009	2815	50	0.362	0.008
Step 3	0.00311	0.00006	0.767	0.010	0.749	0.012	4322	44	0.527	0.007
Step 4	0.00317	0.00007	1.087	0.013	0.729	0.012	4263	28	0.524	0.006
Total	0.00331	0.00006	0.866	0.007	0.692	0.009	3221	57	0.413	0.009
Laser Ablation										
Px1	0.00647	0.00069	1.56	0.05	0.77	0.03	260	9	1.17	0.05
Px2	0.00479	0.00015	0.71	0.05	0.95	0.04	709	94	4.55	0.60
Px3	0.00477	0.00021	1.02	0.03	0.87	0.03	811	20	1.46	0.04
Px4	0.00325	0.00009	0.90	0.04	0.99	0.04	644	21	0.42	0.01
Px5	0.00504	0.00011	1.07	0.04	0.92	0.03	766	19	1.52	0.04
Plag1	0.00681	0.00370					50400	3700	1.30	0.10

755

756

Table 2 - Noble gas abundances for the three separate extraction techniques. Units are mol.g^{-1} for step heating and crushing, and mol.cm^{-3} for laser ablation analyses. Uncertainties are given at the 1σ level. He, Ne and Ar results for step heating are reported in Barrat et al., 2021, and reproduced in Table S2 for reference. Sample masses used for step heating and crushing are 8.3 mg and 185.2 mg respectively.

	^{3}He (x10^{-13})	±	^{21}Ne (x10^{-13})	±	^{40}Ar (x10^{-10})	±	^{84}Kr (x10^{-16})	±	^{132}Xe (x10^{-16})	±	^{4}He (x10^{-13})	±	^{22}Ne (x10^{-13})	±	^{36}Ar (x10^{-15})	±
Step Heating (mol.g^{-1})																
600 °C																
800 °C							29.8	1.1	12.1	1.2						
1000 °C																
1200 °C							86.0	2.7	5.3	0.6						
1400 °C							45.1	1.1	5.7	0.9						
Total							160.8	3.1	23.1	1.6						
Crushing (mol.g^{-1})																
Step 1	0.018	0.001	0.00411	0.00019	0.0137	0.0001	1.02	0.06	0.025	0.012	5.5	0.3	0.0064	0.0003	2.00	0.02
Step 2	0.186	0.013	0.02310	0.00055	0.1365	0.0011	1.56	0.04	0.113	0.032	54.4	3.9	0.0341	0.0009	4.85	0.09
Step 3	0.057	0.004	0.00623	0.00017	0.0425	0.0003					18.3	1.3	0.0083	0.0003	0.98	0.01
Step 4	0.049	0.004	0.00518	0.00019	0.0416	0.0003					15.5	1.3	0.0071	0.0003	0.98	0.01
Total	0.310	0.015	0.03861	0.00064	0.2344	0.0011	2.59	0.07	0.138	0.034	93.7	4.8	0.0558	0.0012	7.28	0.13
Laser Ablation (mol.cm^{-3})																
Px1	512	9	104	2	16.9	1.0					79000	9000	135	6	6500	400
Px2	553	11	109	3	8.7	1.7					115000	4000	114	6	1200	300
Px3	510	10	102	2	46.2	1.9					107000	5000	117	5	5700	300
Px4	549	11	108	2	259	13					169000	6000	109	5	40000	2000
Px5	521	7	101	2	45.2	1.9					103000	3000	109	4	5900	300
Plag1	7	1	10	0.4	833	94					1000	600			1600	200

Table 3 - Xe isotope ratios for step heating and crushing analyses for extractions where measurable amounts of Xe were released. ^{126}Xe was below detection limit (b.d.) for the 800°C step and so is not reported. Uncertainties are given at the 1σ level.

	$^{124}Xe/^{132}Xe$	±	$^{126}Xe/^{132}Xe$	±	$^{128}Xe/^{132}Xe$	±	$^{129}Xe/^{132}Xe$	±	$^{130}Xe/^{132}Xe$	±	$^{131}Xe/^{132}Xe$	±	$^{134}Xe/^{132}Xe$	±	$^{136}Xe/^{132}Xe$	±
Step Heating																
800 °C	0.00308	0.00018	b.d.		0.0687	0.0029	0.965	0.036	0.1425	0.0055	0.786	0.030	0.379	0.014	0.326	0.013
1200 °C	0.01226	0.00074	0.01716	0.00132	0.0928	0.0039	0.923	0.035	0.1391	0.0059	0.848	0.036	0.405	0.017	0.372	0.015
1400 °C	0.00431	0.00041	0.00746	0.00073	0.0858	0.0049	0.912	0.047	0.1544	0.0088	0.766	0.038	0.386	0.021	0.318	0.017
Crushing																
Step 1	0.00421	0.00090	0.00296	0.00056	0.0646	0.0086	0.977	0.114	0.1210	0.0139	0.774	0.085	0.572	0.068	0.499	0.061
Step 2	0.00231	0.00045	0.00341	0.00093	0.0535	0.0064	0.954	0.099	0.1393	0.0148	0.755	0.080	0.534	0.058	0.400	0.045

Table 4 - Kr isotope ratios for step heating and crushing analyses for extractions where measurable amounts of Kr were released. Uncertainties are given at the 1σ level.

	$^{78}Kr/^{84}Kr$	±	$^{80}Kr/^{84}Kr$	±	$^{82}Kr/^{84}Kr$	±	$^{83}Kr/^{84}Kr$	±	$^{86}Kr/^{84}Kr$	±
Step Heating										
800 °C	0.00738	0.00026	0.0372	0.0009	0.1945	0.0045	0.1956	0.0045	0.333	0.007
1200 °C	0.01507	0.00046	0.0688	0.0015	0.2389	0.0052	0.2556	0.0055	0.283	0.006
1400 °C	0.00665	0.00022	0.0409	0.0008	0.2098	0.0036	0.2024	0.0033	0.307	0.005
Crushing										
Step 1	0.0065	0.0003	0.0412	0.0012	0.201	0.005	0.202	0.005	0.311	0.009
Step 2	0.0079	0.0010	0.0459	0.0035	0.207	0.015	0.204	0.016	0.319	0.023

Table 5 - Nitrogen, neon and argon isotopic compositions and abundances for Erg Chech 002, measured via laser heating extraction. Abundances are all reported in mol.g^{-1}, and $\delta^{15}N$ is reported in permille relative to atmosphere.

	^{21}Ne ($x10^{-13}$)	±	^{40}Ar ($x10^{-10}$)	±	N ($x10^{-7}$)	±	$^{20}Ne/^{22}Ne$	±	$^{21}Ne/^{22}Ne$	±	$^{40}Ar/^{36}Ar$	±	$^{38}Ar/^{36}Ar$	±	$\delta^{15}N$ (‰)	±
	(mol.g^{-1})															
Step 1	3.0	0.4	11.3	0.8	1.11	0.04	0.631	0.034	0.693	0.064	19883	1243	0.72	0.03	0.9	0.5
Step 2	3.4	0.4	30.7	1.7	1.66	0.06	0.859	0.042	0.904	0.082	42808	2130	1.58	0.11	5.5	0.5
Step 3	13.9	1.5	41.7	0.7	1.04	0.04	0.837	0.030	0.906	0.080	5263	25	1.55	0.02	45.0	0.6
Bulk	20.3	1.6	83.8	2.0	3.82	0.08	0.802	0.044	0.866	0.077	9088	251	1.50	0.04	15.0	0.5

Table 6 – Deconvolution of the ^{38}Ar and ^{36}Ar composition of EC002 from the sample fragments used for stepped heating and laser heating, into cosmogenic and trapped components. $F^{36}Ar$ is the fraction of ^{36}Ar in the total (^{38}Ar + ^{36}Ar), calculated from $^{38}Ar/^{36}Ar$ by the relationship $F^{36}Ar = (1 + {}^{38}Ar/^{36}Ar)^{-1}$, and f_{cos} is the fraction of cosmogenic (^{38}Ar + ^{36}Ar) within the total, calculated from $F^{36}Ar_{sample} = F^{36}Ar_{cos}f_{cos} + F^{36}Ar_{tr}(1 - f_{cos})$.

				[^{36}Ar] mol.g^{-1}			[^{38}Ar] mol.g^{-1}		
	$^{38}Ar/^{36}Ar$	$F^{36}Ar$	f_{cos}	*total*	*cos*	*tr*	*total*	*cos*	*tr*
Endmembers									
Cosmogenic	1.7	0.37							
Trapped	0.188	0.84							
EC002 samples									
Stepped heating	1.17	0.46	0.81	1.99×10^{-12}	1.29×10^{-12}	6.98×10^{-13}	2.33×10^{-12}	2.20×10^{-12}	1.31×10^{-12}
Laser heating	1.50	0.40	0.94	9.22×10^{-13}	8.02×10^{-13}	1.19×10^{-13}	1.39×10^{-12}	1.36×10^{-12}	2.24×10^{-14}

Supplementary material 1 – Light noble gas isotope and abundance data, compiled from Barrat et al., 2021

	$^{3}He/^{4}He$	±	$^{20}Ne/^{22}Ne$	±	$^{21}Ne/^{22}Ne$	±	$^{40}Ar/^{36}Ar$	±	$^{38}Ar/^{36}Ar$	±
Step Heating										
600 °C	0.00871	0.00007	0.571	0.003	0.613	0.013	1027	14	0.215	0.006
800 °C	0.00741	0.00007	0.506	0.003	0.675	0.014	19702	178	0.791	0.011
1000 °C	0.00601	0.00007	0.624	0.004	0.880	0.019	25097	237	0.997	0.014
1200 °C	0.00448	0.00003	0.807	0.003	0.870	0.018	4699	33	1.218	0.016
1400 °C	0.00105	0.00011	0.613	0.014	0.767	0.019	493	4	0.395	0.005
Total	0.00731	0.00007	0.768	0.002	0.846	0.015	5523	42	1.17	0.015

Table S1 –

	^{3}He ($x10^{-13}$)	±	^{21}Ne ($x10^{-13}$)	±	^{40}Ar ($x10^{-10}$)	±
Step Heating (mol.g^{-1})						
600 °C	4.12	0.28	0.817	0.038	0.18	0.01
800 °C	85.6	5.8	1.088	0.050	17.3	0.6
1000 °C	1.05	0.07	0.844	0.039	13.9	0.5
1200 °C	4.77	0.32	14.849	0.681	77.9	2.4
1400 °C	0.007	0.001	0.093	0.004	0.95	0.03
Total	95.5	5.8	17.700	0.685	110.0	2.5

Table S2 – Sample masses used for step heating and crushing are 8.3 mg and 185.2 mg respectively.

Cut text

Bulk abundances and isotope ratios were calculated using an abundance-weighted average. As shown in Fig. 1, the majority of He was released at the 800°C step, whilst Ne and Ar were predominantly released at 1200°C. This is likely a result of the greater mobility of He at lower temperatures, but may also be due to differential siting of distinct noble gas components within different mineral phases.

Bulk $^{3}He/^{4}He$ is 0.00731 ± 0.00007, which indicates a large contribution of cosmogenic ^{3}He. Bulk Ne isotopes are also strongly cosmogenic, with $^{20}Ne/^{22}Ne$ = 0.768 ± 0.002 and $^{21}Ne/^{22}Ne$ = 0.846 ± 0.015, within the range of expected cosmogenic production ratios for stony meteorites (Eugster & Michel, 1995). There is however a notable variation in the Ne isotopic composition with different temperature releases: low temperature steps 600°C and 800°C show significantly lower $^{20}Ne/^{22}Ne$ and $^{21}Ne/^{22}Ne$ than the major Ne release step at 1200°C. This likely reflects the different cosmogenic production ratios between different mineral phases (as shown in Fig. 2 and discussed in section 4.2.2). Bulk Ar isotopes are strongly enriched in radiogenic ^{40}Ar (produced by decay of ^{40}K), with $^{40}Ar/^{36}Ar$ = 5523 ± 42. Minor releases of Ar at the 800°C and 1000°C temperature steps show even higher $^{40}Ar/^{36}Ar$ of 19,702 ± 178 and 25,097 ± 237, respectively, which is likely a result of preferential Ar release from the K-enriched feldspar minerals at lower temperatures, suggesting that the $^{40}Ar/^{36}Ar$ of the sample is strongly heterogeneous and dependent on the host mineral composition. Bulk measured $^{38}Ar/^{36}Ar$ is close to expected cosmogenic values at 1.17 ± 0.015, but again shows significant variability between extraction steps (Table 1). Bulk abundances of ^{3}He, ^{20}Ne and ^{40}Ar are 95.50 ± 5.77 $x10^{-13}$ $mol.g^{-1}$, 16.05 ± 0.69 $x10^{-13}$ $mol.g^{-1}$, and 110.00 ± 2.53 $x10^{-10}$ $mol.g^{-1}$ respectively.

815
816